Formation of Forsterite by Silicification of Dolomite during Contact Metamorphism

JOHN M. FERRY[1]*, TAKAYUKI USHIKUBO[2] AND JOHN W. VALLEY[2]

[1]DEPARTMENT OF EARTH AND PLANETARY SCIENCES, JOHNS HOPKINS UNIVERSITY, BALTIMORE, MD 21218, USA

[2]WiscSIMS, DEPARTMENT OF GEOSCIENCE, UNIVERSITY OF WISCONSIN, MADISON, WI 53706, USA

Four samples that experienced the infiltration-driven reaction 2 dolomite $+ SiO_2(aq) =$ forsterite $+ 2$ calcite $+ 2$ CO_2 exhibit correlations among forsterite crystal morphology, size, number density (number of Fo crystals per cm^3 Fo), and oxygen isotope ratio ($\delta^{18}O$). The $\delta^{18}O$ of coexisting forsterite, calcite, and dolomite were determined by in situ *ion microprobe analysis with a spatial resolution of $\sim15\,\mu m$. Sample KP1L from the Twin Lakes pendant, Sierra Nevada, California, contains blocky forsterite with the largest average crystal size and the lowest crystal number density. Forsterite and calcite are uniform in $\delta^{18}O$ with the measured fractionation consistent with equilibrium at the temperature inferred for the reaction ($595°C$). Sample B4L from the Beinn an Dubhaich aureole, Scotland, contains tabular forsterite with intermediate average size and number density. Forsterite and calcite are uniform in $\delta^{18}O$ but the measured fractionation is smaller than the equilibrium value at the temperature inferred for the reaction ($680°C$). Samples B1W and B43A from the Beinn an Dubhaich aureole contain rounded forsterite with the smallest average size and largest number density. Forsterite has variable $\delta^{18}O$ differing among grains by up to $7·4‰$ in single samples and by up to $3·1‰$ within a single grain, precluding isotope equilibrium with calcite and dolomite. Crystal morphology, size, number density, $\delta^{18}O(Fo)$, and $\Delta^{18}O(Cal–Fo)$ can be understood in terms of the interplay between reaction affinity (A) and Peclet Number (Pe) during formation of forsterite (KP1L: low A, high Pe; B4L: intermediate A and low Pe; B43A: high A, low Pe; B1W: high A, increasing Pe). Differences in A were controlled by variations in X_{CO_2} in the infiltrating fluid. Differences in Pe were controlled by variations in fluid flux and/or width of the reaction zone. If the infiltrating fluid is initially quartz-saturated, phase equilibria require that development of forsterite and periclase from dolomite during contact metamorphism must be preceded by reactions that produce diopside, wollastonite, and/or other skarn minerals upstream.*

INTRODUCTION

From the standpoint of petrology, the essence of metamorphism is the chemical reaction among minerals and fluid. Surprisingly, much remains to be understood about metamorphic mineral reactions, including the role of metasomatism, how and to what extent reactions are overstepped, the controls on the textures of mineral products, and the grain-scale redistribution of isotopes during reaction. Recently, the formation of forsterite during contact metamorphism of dolomite has emerged as a kind of 'standard' in the study of reactions for two reasons. First, mineral reactants and products have simple chemical compositions, very limited chemical variability, and well-defined thermodynamic properties. Second, the formation of forsterite in dolomite marble involves a range of fluid compositions, produces a variety of olivine textures, and results in different distributions of stable isotopes between reactants and products. Studies of the formation of forsterite therefore can reveal how mineral reactions are linked to fluid–rock interaction, microstructures, and isotope transport during metamorphism.

Several types of reaction have been proposed for the formation of forsterite during contact metamorphism of carbonate rocks. The traditional ones are isochemical reactions that produce forsterite (Fo, Mg_2SiO_4) and calcite (Cal, $CaCO_3$) from dolomite [Dol, $CaMg(CO_3)_2$] and

*Corresponding author. Telephone: (410) 516-8121. Fax: (410) 516-7933. E-mail: jferry@jhu.edu

either tremolite [Tr, $Ca_2Mg_5Si_8O_{22}(OH)_2$] or diopside (Di, $CaMgSi_2O_6$):

$$Tr + 11\ Dol = 8\ Fo + 13\ Cal + 9\ CO_2 + H_2O \qquad (1)$$

$$Di + 3\ Dol = 2\ Fo + 4\ Cal + 2\ CO_2 \qquad (2)$$

(e.g. Bowen, 1940; Skippen, 1974; Moore & Kerrick, 1976; Ferry, 1994; Roselle, 1997; Cook & Bowman, 2000). The occurrence of coexisting $Tr + Dol + Fo + Cal$ and $Di + Dol + Fo + Cal$ is direct evidence for reactions (1) and (2) in specific instances of contact metamorphism (e.g. Ferry, 1996a; Ferry et al., 1998, 2002). Some rocks with reactants and products of reaction (1) and (2) contain Cal that records a Cal–Dol temperature (T) within the range over which reaction (1) or (2) is stable (e.g. Ferry, 1996b, 2001; Ferry et al., 1998). In these cases, reactions (1) and (2) probably proceeded close to equilibrium.

There is evidence, however, that the reaction that produced Fo in other instances involved a source of silica other than Tr or Di and that reaction occurred far from equilibrium (Roselle et al., 1997; Müller et al., 2004). Calcite inclusions in Fo from dolomite marbles that record Cal–Dol T higher than the T at which the isobaric univariant assemblages $Tr + Dol + Fo + Cal$ and $Di + Dol + Fo + Cal$ can coexist at equilibrium with CO_2–H_2O fluid (Ferry, 2001) are also evidence that Fo formed either by reactions other than (1) and (2) and/or at conditions far from equilibrium. Based on oxygen isotope data and textures of coexisting Fo, Cal, and Dol, Müller et al. (2004) concluded that Fo formed in the Ubehebe Peak aureole by the metastable reaction

$$2\ Dol + SiO_2 = Fo + 2\ Cal + 2\ CO_2 \qquad (3)$$
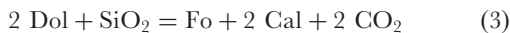
where the proposed source of SiO_2 was quartz (Qtz).

Several studies have documented that Fo may form during contact metamorphism by reaction (3), but at $a_{SiO_2} < 1$ with reactant SiO_2 supplied as dissolved silica by infiltration of dolomite by aqueous fluid. Specific occurrences include Fo–Cal veins in dolomite marble from the Bergell aureole (Bucher-Nurminen, 1981; Bucher, 1998; Begue, 2008) and pervasive development of Fo in dolomite marble from the Adamello and Beinn an Dubhaich aureoles (Bucher-Nurminen, 1982; Holness, 1997). This study focuses on the formation of Fo by silicification of dolomite for two reasons. First, wide ranges of morphology, crystal size, and crystal number density of Fo in contact metamorphosed marbles are readily explained by a silicification reaction. Using in situ ion microprobe analyses, we show for the first time for any metamorphic reaction a diversity of ways in which oxygen isotopes are redistributed among reactants and products at the grain scale. Second, this diversity in isotope behavior is also explained by formation of Fo by silica metasomatism.

GEOLOGICAL SETTINGS

Samples of Fo marble and associated rocks were collected from the Twin Lakes pendant, central Sierra Nevada, California, USA, and from the Beinn an Dubhaich aureole, Isle of Skye, Scotland as part of earlier studies (Davis & Ferry, 1993; Ferry & Rumble, 1997; Wing et al., 2000). The Twin Lakes pendant is mostly composed of calc-silicate hornfels and marble (Chesterman, 1942; Kerrick et al., 1973). Contact metamorphism was caused by intrusion of the Mount Givens and Dinkey Creek granodiorites, which have $^{206}Pb/^{238}U$ zircon ages of 88–92 Ma and 104 Ma, respectively (Stern et al., 1981). This paper focuses on the marbles. They contain combinations of Cal, Dol, Fo, Di, Tr, brucite after periclase (Per), humite minerals, and phlogopite (Chesterman, 1942; Kerrick et al., 1973; Davis & Ferry, 1993). Prograde mineral reactions in both marble and calc-silicate hornfels were driven by infiltration of rocks by H_2O-rich fluids. Skarns developed along some contacts between marble and granodiorite (Chesterman, 1942).

The geology, petrology, and geochemistry of the Beinn an Dubhaich aureole have been summarized by Holness (1990, 1992, 1997), Holness et al. (1991), and Holness & Fallick (1997). Contact metamorphism occurred with emplacement of the Beinn an Dubhaich granite at ~54 Ma (Moorbath & Bell, 1965). This paper focuses on metamorphism of the Balnakiel Formation, a siliceous dolomite composed of 85–99% Dol. Where Dol reacted to $Per + Cal$ during metamorphism, the rock is now Cal–brucite marble. Holness (1990, 1992) mapped isograds in the aureole based on the appearance of talc (Tlc), Tr, Di, Fo, and Per in marbles. Phase equilibria and stable isotope geochemistry document infiltration of the aureole by chemically reactive, H_2O-rich fluids probably derived from the granite (Holness, 1990, 1992, 1997; Ferry & Rumble, 1997; Holness & Fallick, 1997). Skarns developed along some contacts between marble and granite (Tilley, 1948, 1951).

SAMPLE SELECTION AND METHODS OF INVESTIGATION
Sample selection

The study focuses primarily on four samples: KP1L from the Twin Lakes pendant and samples B4L, B43A, and B1W from the Beinn an Dubhaich aureole. Two other samples from the Twin Lakes pendant, KP1B and KP1K, are considered to a lesser extent. All samples from the Twin Lakes pendant are from outcrop 1 of Davis & Ferry (1993). Sample KP1L is a Fo–Cal vein in Dol marble. Samples KP1B and KP1K are Di–Cal–Fo–Dol and Dol marbles respectively. Samples KP1B and KP1L were collected at locations illustrated in fig. 2 of Davis & Ferry (1993); sample KP1K was collected ~1 m from sample

KP1L. Sample B4L is a Cal–Dol–Fo marble collected along an extension of traverse 4, 137 m SW from sample 4O of Ferry & Rumble (1997, figs 1 and 4). Sample B43A is a drill core that contains both Dol and Fo–Cal marbles collected at location 3 of Ferry & Rumble (1997, fig. 3). Sample B1W is a Dol marble with wispy Fo–Cal segregations collected within ∼3 m of the dolomite–pluton contact at the eastern tip of the granite (eight-digit UK National Grid reference 62061971).

Petrography, mineral analysis, and textural analysis

Samples were imaged both in polished thin sections and in 2·54 cm diameter circular rock disks (for ion microprobe analysis) using transmitted and reflected light microscopy and backscattered electron imaging (BSE) with the JEOL JXA-8600 electron microprobe at Johns Hopkins University and with the Hitachi S3400N variable pressure scanning electron microscope (SEM) in the Department of Geoscience at the University of Wisconsin, Madison. Mineral compositions were analyzed with the electron microprobe at Johns Hopkins University using wavelength-dispersive spectrometry, natural and synthetic silicate and carbonate mineral standards, and a ZAF correction scheme (Armstrong, 1988). Modes were measured by counting ≥ 2000 points with BSE imaging at Johns Hopkins.

The Fo crystal number density (number of Fo crystals per cm^3 Fo) was measured in rock disks of samples KP1L, B4L, B43A, and B1W from 1–5 reflected light images of representative areas. Within each image the number of Fo crystals was counted, and the total area of Fo was measured using an image analysis program. A total of 200–1100 crystals was counted per sample. Following Roselle *et al.* (1997), crystal numbers per unit area were converted to crystal numbers per unit volume of Fo by raising the area number density to the power of 1·5. The volume number density was also referenced to 1 mole Fo for comparison with values reported by Roselle *et al.* (1997). Average crystal size of Fo was calculated as the inverse of the cube root of crystal number density on a volume basis.

Oxygen isotope analysis

The stable isotope composition of bulk carbonate in samples from the Twin Lakes pendant was analyzed in the laboratory of A. J. Kaufman using powders extracted from sawn slabs with a 1 or 2 mm diameter diamond-tipped drill as described in more detail by Penniston-Dorland & Ferry (2006) and Carmichael *et al.* (2008). Values of $\delta^{18}O$ are reported relative to VSMOW. Frequent analyses of separate aliquots of calcite standard NBS-19 indicate that analytical precision for oxygen isotopes was *c.* ± 0.1‰ (1 standard deviation, SD) or better.

Sample mounts for ion microprobe analysis were prepared as 2·54 cm diameter, 5 mm thick rock disks polished with special care to minimize surface relief (Kita *et al.*, 2009). Calcite and Dol standards were mounted in the centers of all samples. An additional sample mount was prepared containing Cal, Do, Fo, and Qtz standards. Areas for analysis were located in almost all cases within ∼5 mm of the center of the mount and documented both with BSE imaging using the Hitachi S3400N electron microscope and with reflected light microscopy.

In situ oxygen isotope analyses of Cal, Dol, and Fo in samples KP1L, B4L, B43A, and B1W were obtained with the CAMECA ims-1280 ion microprobe in the WiscSIMS Laboratory, Department of Geoscience at the University of Wisconsin, Madison, using operating and analytical conditions described in detail by Kita *et al.* (2009) and Ferry *et al.* (2010). The primary ion beam was focused to ∼15 µm on the sample surface. Data were corrected for instrumental bias using either UWC1 Cal standard ($\delta^{18}O = 23.36$‰ VSMOW) or UWC3 Cal standard ($\delta^{18}O = 12.49$‰, Kozdon *et al.*, 2009) for Cal, UW6220 Dol standard ($\delta^{18}O = 22.72$‰) for Dol, and San Carlos olivine ($\delta^{18}O = 5.32$‰, Kita *et al.*, 2010) for Fo. The Cal standard in each sample was measured four times every 10–12 unknown analyses. The bias correction was based on the average of the four standard analyses made before and after the group of unknowns (eight total analyses of the standard). The average spot-to-spot reproducibility, or 'analytical uncertainty' in the terminology of Kita *et al.* (2009), of analyses of unknowns was considered ± 2 SD of the eight bracketing calcite standard analyses. For all $\delta^{18}O$ measurements made in the analytical session, the average 2 SD was 0·37‰ (range 0·14–0·73‰). Oxygen isotope ratios were normalized to VSMOW and reported as $\delta^{18}O$. Values of $\delta^{18}O$ of Cal and Dol were corrected for Mg content using the measured difference in bias between Cal and Dol standards and assuming a linear dependence of bias on the mole fractions of $MgCO_3$ and $CaMg(CO_3)_2$ in Cal and Dol, respectively (Valley & Kita, 2009). No correction of bias was necessary for the difference in composition between the San Carlos olivine standard and analyzed Fo in the samples (Kita *et al.*, 2010).

Every ion microprobe analysis pit was examined by BSE imaging to evaluate whether any were contaminated by inclusions of other minerals or were in a potentially problematic textural site. Only one such analysis pit was identified in the samples examined for this study. The pit lies along a fracture, and the analytical result is reported but considered suspect.

Phase equilibrium calculations

Thermodynamic calculations used the Berman (1988; updated June 1992) database and the Kerrick & Jacobs (1981) equation of state (EOS) for CO_2–H_2O fluids. The calculations assumed that Fo, Di, Dol, Cal, and Per are

pure substances with idealized compositions. Molar volumes of minerals were taken from the Holland & Powell (1998) database.

MINERALOGY AND MINERAL CHEMISTRY

Samples KP1L, B4L, B43A, and B1W are mostly composed of Fo, Cal, and Dol in various proportions with variable minor or trace quantities of Di, Tr, phlogopite, spinel, apatite, and Fe sulfide (Table 1). Forsterite in the four samples is partially altered to an intergrowth of serpentine and brucite. Sample KP1B contains mostly Di with lesser amounts of Cal and Fo and minor Dol. Sample KP1K contains Dol and <0·05% Cal, and is devoid of Fo and Di.

All analyzed minerals are close to pure substances with limited chemical variation (Table 2). Forsterite is nearly pure Mg_2SiO_4 with $Mg/(Mg + Fe) \geq 0.996$. Dolomite has 1·016–1·033 Ca atoms per formula unit (p.f.u.) and $Mg/(Mg + Fe) \geq 0.997$. Calcite is a Ca–Mg solid solution. Matrix Cal has 0·023–0·035 Mg atoms p.f.u. As has been observed in other samples worldwide (Ferry, 2001), Cal inclusions in Fo can have significantly higher Mg contents, up to 0·070–0·106 Mg atoms p.f.u. in samples KP1B, B1W,

and B43A. Diopside in sample KP1B has the composition $Ca_{0.99}Mg_{1.01}Si_{2.00}O_6$ (Davis & Ferry, 1993).

TEMPERATURE AND PRESSURE

The T at which Fo formed in samples B43A and B1W (655°C and 690°C, respectively) was calculated from the composition of calcite inclusions in Fo (Table 2) following Anovitz & Essene (1987), assuming the Cal inclusions were in equilibrium with Dol when Fo formed (Table 3). Samples KP1L and B4L do not contain Fo with Cal inclusions suitable for analysis. The T of Fo formation in sample KP1L was taken as 595°C, that recorded by the composition of Cal inclusions in Fo from sample KP1B collected 70 m away (Table 2). The T of Fo formation in sample B4L was taken as 680°C, that recorded by the composition of Cal inclusions in Fo from sample B4K collected 34 m away along the same sample traverse.

Estimated pressure during metamorphism in the Beinn an Dubhaich aureole is 500 bars (Ferry & Rumble, 1997). Pressure during metamorphism in the Twin Lakes pendant was earlier estimated from equilibria among Tr, Fo, Di, Cal, and Dol in marble and among wollastonite, grossular, anorthite, and Qtz in hornfels (Davis & Ferry, 1993). It has since been recognized, however, that Tr and

Table 1: Mineral assemblages, modes, and Ca/Mg ratios of samples investigated

Sample:	KP1B	KP1K	KP1L	B1W	B4L	B43A
Location:	TL	TL	TL	BaD	BaD	BaD
Rock type:	Di–Cal–Fo–Dol marble	Dol marble	Cal–Fo vein in Dol marble	Dol–Cal–Fo marble	Dol–Cal-Fo marble	Cal–Fo vein in Dol marble
Dolomite (Dol)	3·02	99·76	33·04	81·93	26·20	49·01
Calcite (Cal)	25·98	tr	43·29	10·86	45·19	32·97
Forsterite	14·62	0	20·91	4·42	25·23	14·02
Serpentine + brucite	1·15	0·19	2·76	2·64	0·82	3·96
Phlogopite	0	0·05	0	0·10	1·79	0
Diopside	55·23	0	0	0	0·05	0
Spinel	0	0	0	0	0·43	0
Apatite	0	0	0	tr	0·05	0
Fe-sulfide	0	0	0	0	0·24	0
Tremolite	0	0	0	0·05	0	0
% Cal in matrix/wall rock	n.a.	n.a.	0·2	<0·1	n.a.	0·2
% Dol in vein/segregation	n.a.	n.a.	1·5	1·0	n.a.	6·8
Molar Ca/Mg, less Dol*	0·98 ± 0·07	n.a.	1·05 ± 0·10	0·98 ± 0·20	0·96 ± 0·09	1·11 ± 0·13
Molar Ca/Mg, dolomite	1·03	1·05	1·05	1·07	1·06	1·04

Values in vol. %; tr, <0·05%; n.a., not applicable. TL, Twin Lakes pendant; BaD, Beinn an Dubhaich aureole. Di, diopside; Cal, calcite; Fo, forsterite; Dol, dolomite.
*Molar Ca/Mg of rock, omitting dolomite, calculated from modes and mineral compositions. Uncertainty is ±2 SD from point-counting errors.

Table 2: Mineral compositions (cations per formula unit) in samples investigated

	Matrix calcite				
Sample:	KP1B	KP1L	B1W	B4L	B43A*
Ca	0·977	0·965	0·970	0·971	0·974
Mg	0·023	0·035	0·030	0·029	0·026
Fe	0	0	0	0	0
Mn	0	0	0	0	0
Oxide sum	56·07	56·05	55·75	56·03	56·33

	Calcite inclusion in forsterite with maximum Mg content		
Sample:	KP1B	B1W	B43A
Ca	0·928	0·893	0·908
Mg	0·070	0·106	0·092
Fe	0·001	0·001	0
Mn	0·001	0	0
Oxide sum	55·44	55·85	55·58
T (°C)†	595	690	655

	Forsterite				
Sample:	KP1B	KP1L	B1W	B4L	B43A
Mg	1·996	1·991	1·985	1·985	1·992
Fe	0·009	0·007	0·009	0·012	0·007
Mn	0	0·001	0·001	0·001	0
Si	0·997	1·000	1·001	1·000	0·999
Oxide sum	100·25	99·88	99·72	100·05	100·40

	Dolomite					
Sample:	KP1B	KP1K	KP1L	B1W	B4L	B43A
Ca	1·016	1·024	1·022	1·033	1·025	1·019
Mg	0·984	0·975	0·977	0·965	0·971	0·980
Fe	0	0·001	0·001	0·002	0·003	0·001
Mn	0	0	0	0	0·001	0
Oxide sum	52·41	52·62	52·38	52·27	52·23	52·27

Values in atoms per formula unit: calcite, 1 oxygen atom (less CO_2); forsterite, 4 oxygen atoms; dolomite, 2 oxygen atoms (less CO_2). Oxide sums for calcite and dolomite are less CO_2.
*Excluding analyses of turbid, altered calcite.
†T calculated following Anovitz & Essene (1987), rounded to nearest 5°C.

Table 3: Forsterite crystal number density, crystal size, and morphology; oxygen isotope compositions of forsterite, calcite, and dolomite

Sample:	KP1L	B4L Matrix	B43A	B1W
Fo number density (cm^{-3} Fo)[1]	1.5×10^5	9.6×10^6	2.2×10^7	5.5×10^7
Fo number density (mol^{-1} Fo)[1]	6.7×10^6	4.2×10^8	9.4×10^8	2.4×10^9
Average Fo size (μm)[2]	190	47	36	26
Fo morphology	blocky	tabular	bead-like[7]	bead-like
$\delta^{18}O$(Fo) (‰, VSMOW)[3]	6.8 ± 0.2	18.8 ± 0.2	12.1–15.0	9.8–17.2
$\delta^{18}O$(Cal) (‰, VSMOW)[3]	11.0 ± 0.1	21.4 ± 0.2[8]	15.9–18.2[9]	18.3–19.9
$\delta^{18}O$(Dol) (‰, VSMOW)[3]	8.9–19.0	21.0 ± 0.3	17.4 ± 0.2	18.7 ± 0.1
Measured $\Delta^{18}O$(Cal-Fo) (‰)[4]	4.2 ± 0.2	2.6 ± 0.3[8]	Inhomog.	Inhomog.
Inferred T of reaction (3) (°C)[5]	595	680	655	690
Equilibrium $\Delta^{18}O$(Cal-Fo) (‰)[6]	4.4	3.6	3.8	3.5

[1]Number of Fo crystals per cm^3 Fo or number of Fo crystals per mol Fo.
[2]Computed as the cube root of the inverse of number density on a volume basis.
[3]A single number is the weighted mean value when the analyzed mineral is homogeneous within error of measurement or homogeneous with the exception of one or two outliers. The uncertainty is the 95% confidence interval of the weighted mean. A range of measured values is given when the mineral is inhomogeneous.
[4]Measured ^{18}O–^{16}O fractionation between Cal and Fo calculated as the difference between the weighted mean values of $\delta^{18}O$; uncertainty is the 95% confidence interval. No value is reported when Fo and Cal are inhomogeneous in $\delta^{18}O$.
[5]From Cal–Dol thermometry (see text).
[6]Equilibrium ^{18}O–^{16}O fractionation between Cal and Fo computed from Chacko *et al.* (2001) for inferred T of reaction (3).
[7]A few large Fo grains have angular rather than rounded shapes.
[8]Excluding one anomalous analysis of Cal on a crack.
[9]Excluding analyses of turbid Cal.

grossular often develop during retrograde rather than prograde contact metamorphism of carbonate rocks (Ferry, 1996a; Ferry *et al.*, 1998, 2002). Assuming Tr and grossular are prograde minerals leads to *P* estimates that are too high. The new preferred value of *P* is 1800 ± 500 bars, based on the range (1360–2270 bars) over which Fo, Di, Dol, and Cal in sample KP1B could coexist with CO_2–H_2O fluid at 595°C in the absence of Tr (Table 2).

FORSTERITE OCCURRENCE AND TEXTURE
Forsterite occurrence
Forsterite occurs differently in samples KP1L, B4L, B43A, and B1W. In sample KP1L, Fo and Cal occur in a vein, ~1.5 cm wide, bounded on both sides by Dol marble that is devoid of silicate minerals and that contains 0.2 modal % Cal (Fig. 1, Table 1). The Fo–Cal vein contains 1.5% Dol that is concentrated at the vein–marble contact, typically in optical continuity with Dol in the marble. The vein–marble contact has a distinctive scalloped appearance (Fig. 2a). Tips of the cusps of the scallops correspond to penetration of Cal along grain boundaries in the Dol marble.

Forsterite exhibits two modes of occurrence in sample B4L (Fig. 3a and b). One occurrence is in Fo–Cal veinlets that have the same texture as the macroscopic vein in sample KP1L except for their smaller thickness (several hundred micrometers). Forsterite grains in the veinlets are mostly several tens of micrometers in diameter or less (Fig. 3b). The second mode of occurrence of Fo in sample B4L is as larger tabular crystals, up to ~1–2 mm long, in the matrix between adjacent veinlets (Fig. 3b and c).

Sample B43A is a 9.8 cm long drill core that captures a sharp contact between Dol marble and Fo–Cal marble. Dolomite marble contains 0.2% Cal and is devoid of silicate minerals (Table 1). The Fo–Cal marble (Fig. 4) contains 6.8% Dol. The contact between Dol and Fo–Cal marbles displays the same scalloped pattern as observed in sample KP1L.

Forsterite in sample B1W occurs in wispy, anastomosing Fo–Cal segregations in a matrix of Dol marble (Fig. 5a). The dolomite matrix contains <0.1% Cal (Table 1) and only traces of Fo adjacent to the segregations. The segregations contain 1.1% Dol. The contact between the Fo–Cal segregations and the matrix Dol marble is scalloped like the vein–marble contact in sample KP1L (Fig. 5b). The Fo–Cal segregations in sample B1W therefore are

petrographically similar to the vein in sample KP1L except for their irregular rather than planar shape.

Forsterite crystal number density, average crystal size, and morphology

Table 3 summarizes the crystal number density, average crystal size, and morphology of Fo in samples KP1L, B4L, B43A, and B1W. Data for sample B4L refer to the matrix between Fo–Cal veinlets. Crystal number density varies by over two orders of magnitude between $1{\cdot}5 \times 10^5\,\mathrm{cm}^{-3}$ in sample KP1L and $5{\cdot}5 \times 10^7\,\mathrm{cm}^{-3}$ in sample B1W. Correspondingly, average Fo crystal size varies between $190\,\mu\mathrm{m}$ in sample KP1L and $26\,\mu\mathrm{m}$ in sample B1W.
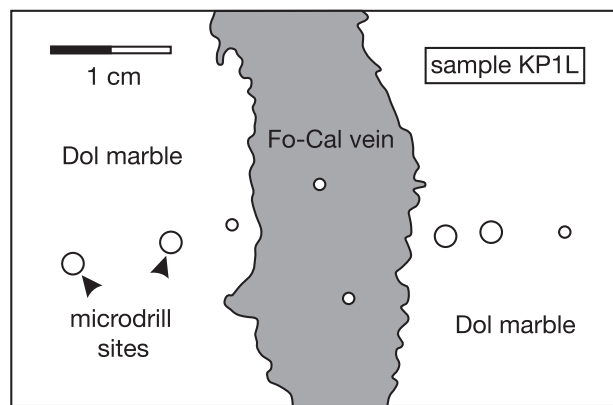
Fig. 1. Tracing of a scanned image of a polished slab of sample KP1L from the Twin Lakes pendant. The location of the Fo–Cal vein was revealed by staining of Cal with alizarin red. The contact between Fo–Cal vein and Dol marble is sharp but scalloped. Circles are the sampling sites for the conventional bulk stable isotope analyses in Fig. 6a.

Forsterite in sample KP1L occurs as relatively large, blocky, subhedral grains up to $\sim$500 μm in diameter (Fig. 2b). Forsterite in the matrix of sample B4L has a tabular morphology with single grains up to $\sim$1–2 mm long but no more than $\sim$100 μm thick (Fig. 3c). Forsterite in samples B43A and B1W occurs either mostly (B43A) or exclusively (B1W) as small, rounded, bead-like grains typically several tens of micrometers in diameter (Figs 4 and 5b). Forsterite in the veinlets in sample B4L exhibits the same bead-like morphology (Fig. 3b). A few Fo grains in sample B43A are larger and angular (Fig. 4).

The tabular morphology of Fo in the matrix of sample B4L and the bead-like morphology of Fo grains in samples B43A and B1W and in the veinlets of sample B4L are the same as Fo morphologies described by Roselle *et al.* (1997) in Fo–Cal–Dol marbles from the Ubehebe Peak aureole. Similar to sample B4L of this study (Fig. 3b), Roselle *et al.* (1997) reported that hand specimens from the Ubehebe Peak aureole may contain Fo with both tabular and bead-like morphologies that occur in spatially segregated groups. Similar to the samples in this study (Table 3), Roselle *et al.* (1997) also observed that Fo with bead-like morphology occurs in a higher crystal number density than Fo with tabular morphology.

OXYGEN ISOTOPE ANALYSES OF FORSTERITE, CALCITE, AND DOLOMITE
Bulk analyses of carbonate

Oxygen isotope analyses of Cal and Dol by conventional millimeter-scale methods along traverses across the Fo–Cal vein in sample KP1L and across the contact
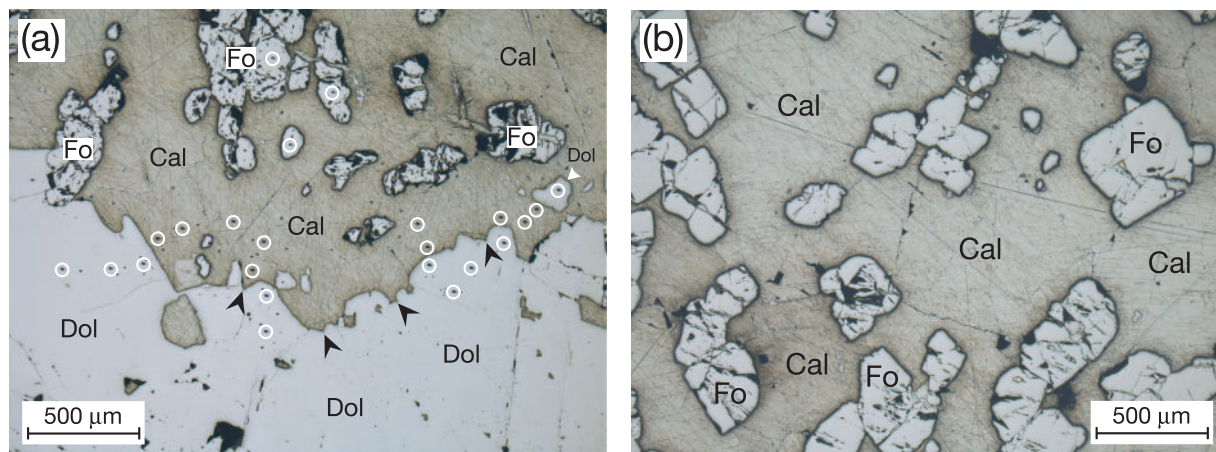

Fig. 2. Reflected light photomicrographs of sample KP1L. Forsterite occurs in a macroscopic Fo–Cal vein developed in Dol marble. (a) The vein–marble contact is scalloped with cusps (several identified by black arrowheads) corresponding to penetration of Cal along Dol grain boundaries. Rare Dol grains in the vein (example indicated by white arrowhead) are in optical continuity with Dol in adjacent wall rock. Black spots within white circles are $\sim$15 μm diameter pits left from *in situ* measurements of δ^{18}O by ion microprobe. (b) In the center of the vein, Fo occurs as relatively large blocky crystals set in a Cal matrix devoid of Dol.
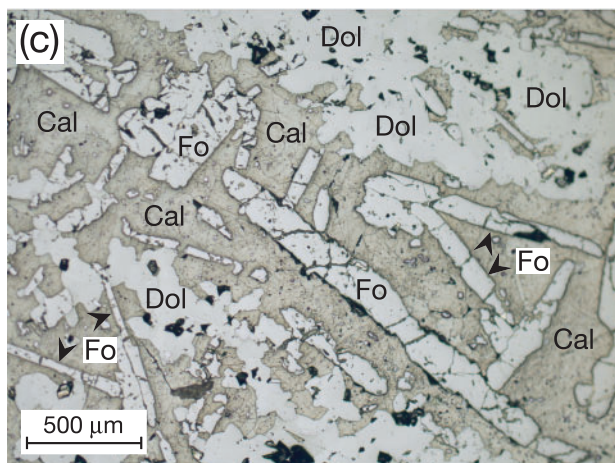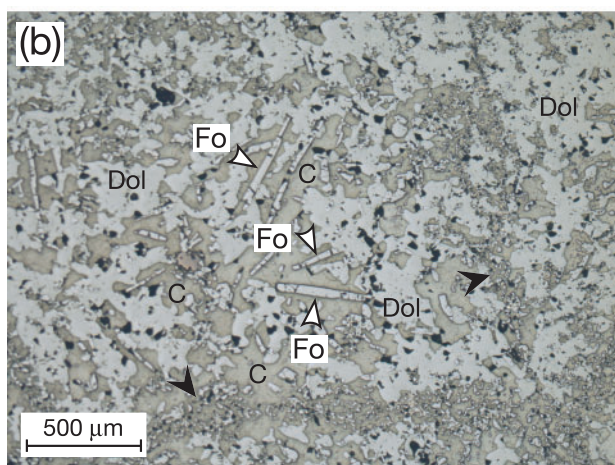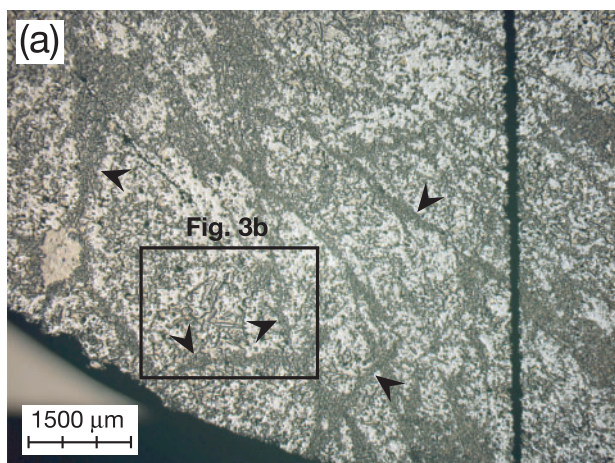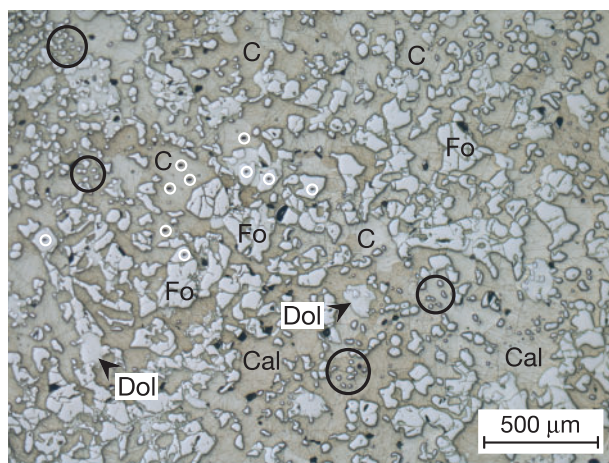
Fig. 4. Reflected light photomicrograph of the center of the Fo–Cal vein in sample B43A. Most Fo grains are rounded, bead-shaped crystals <100 μm in diameter (several clusters appear as high-relief grains within the black circles). Some Fo also occurs as larger, irregular or rounded grains up to several hundred micrometers in diameter (several examples labeled). Black spots within white circles are the same as in Fig. 2a.

between Dol and Fo–Cal marbles in sample B43A are illustrated in Fig. 6. Calcite in the vein in sample KP1L has $\delta^{18}O$ 10–11‰ less than that of Dol more than ∼1 cm distant from the vein–marble contact (Fig. 6a). Similarly, Cal in the Fo–Cal marble of sample B43A more than ∼1 cm distant from the contact has $\delta^{18}O$ up to 8–9‰ less than that of Dol away from the contact (Fig. 6b). Dolomite in sample KP1K and the mixture of Cal and Dol in sample KP1B have a bulk $\delta^{18}O$ of 7·3‰ and 21·5‰, respectively.

Grain-scale analyses of forsterite, calcite, and dolomite

The *in situ* grain-scale oxygen isotope analyses of Fo, Cal, and Dol in samples KP1L, B4L, B43A, and B1W are summarized in Fig. 7 and Table 3.

Measured $\delta^{18}O(Dol)$ in sample KP1L varies by >10‰ both between and within grains (Fig. 7a, Table 3). The lowest values of $\delta^{18}O(Dol)$ are texturally associated with healed fractures, observed in cathodoluminescence and transmitted light microscopy, but not with grain boundaries (Ferry *et al.*, 2010). In contrast, Fo and Cal in the vein have uniform $\delta^{18}O$ within error of measurement both adjacent to the vein–marble contact and in the vein interior (Fig. 7a, Table 3). The measured oxygen isotope fractionation between Cal and Fo, $\Delta^{18}O(Cal-Fo) = 4\cdot2 \pm 0\cdot2$‰, is within error of the equilibrium value (4·4‰) at the

Fig. 3. Reflected light photomicrographs of sample B4L. (a) One occurrence of Fo is in a network of intersecting microscopic Fo–Cal veinlets (darker gray; several indicated by black arrowheads). The area within the rectangle is enlarged in (b). Thick, vertical, black line is a scratch used for navigation during ion microprobe analysis. The edge of the ion microprobe mount is visible in the lower left-hand corner of the photograph. The areas analyzed by ion microprobe are located outside the field of view within 5 mm of the center of the sample mount. (b) A second occurrence of Fo is as tabular crystals (several indicated by white arrowheads) coexisting with Cal (C) and

Dol between Fo–Cal veinlets (indicated by black arrowheads). Forsterite crystals appear rod-shaped in cross-section within the field of view. (c) Representative matrix area between Fo–Cal veinlets. Forsterite occurs as tabular crystals, several tens of micrometers thick and up to ∼1–2 mm in length. Fo coexists with Cal and Dol.
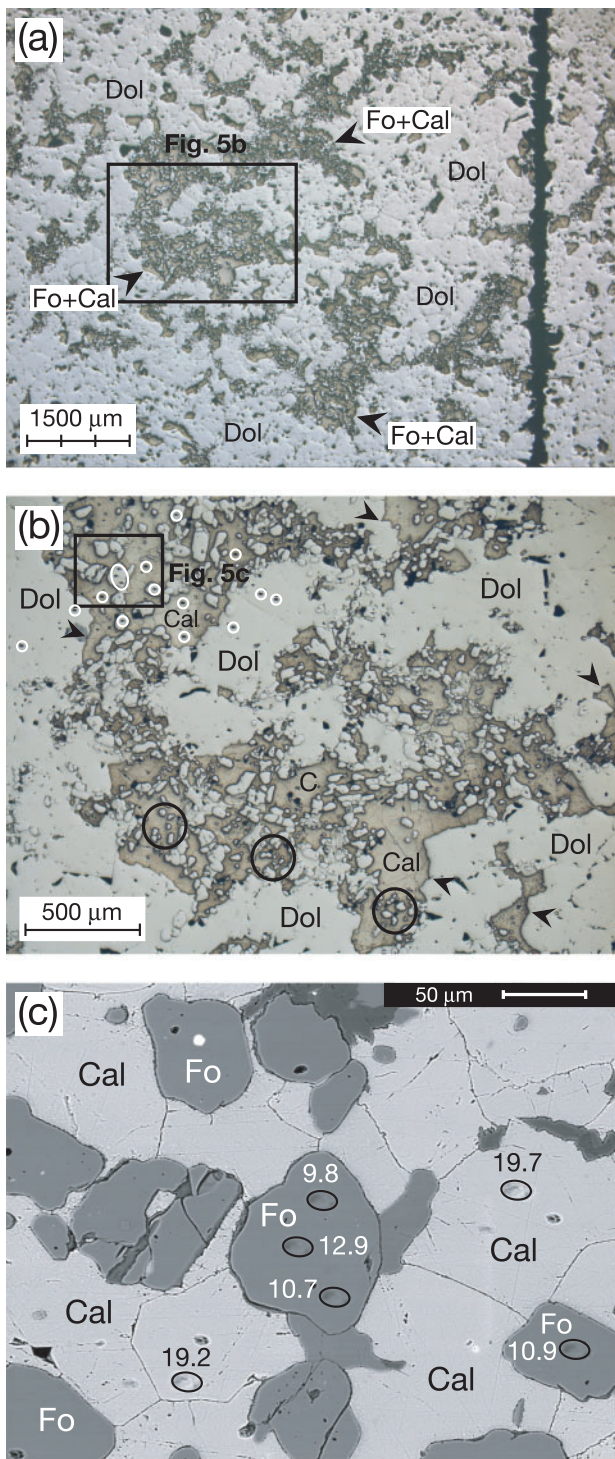
Fig. 5. Reflected light photomicrographs (a, b) and backscattered electron micrograph (c) of sample BlW. (a) Forsterite occurs in wispy, anastomosing Fo–Cal segregations (several indicated by black arrowheads). The area within the rectangle is enlarged in (b). Thick, vertical, black line is the same as in Fig. 3a. (b) Most Fo occurs as rounded, bead-shaped crystals <100 μm in diameter (several clusters appear as high-relief grains within the black circles). The contact between the Fo–Cal segregation and surrounding Dol matrix is scalloped with cusps (several identified by black arrowheads)

corresponding to penetration of Cal along Dol grain boundaries. Black spots within white oval and circles are the same as in Fig. 2a. The area within the black rectangle is enlarged in (c). (c) Enlarged view of the isotopically zoned Fo crystal in sample BlW showing locations of pits left from *in situ* measurements of $\delta^{18}O$ by ion microprobe (black ovals). White numbers are measured values of $\delta^{18}O$ of Fo (‰, VSMOW); black numbers are $\delta^{18}O$ of Cal. Some Fo grains are partly altered to an intergrowth of serpentine + brucite. Bright mineral inclusion in Fo grain at top of image is apatite.
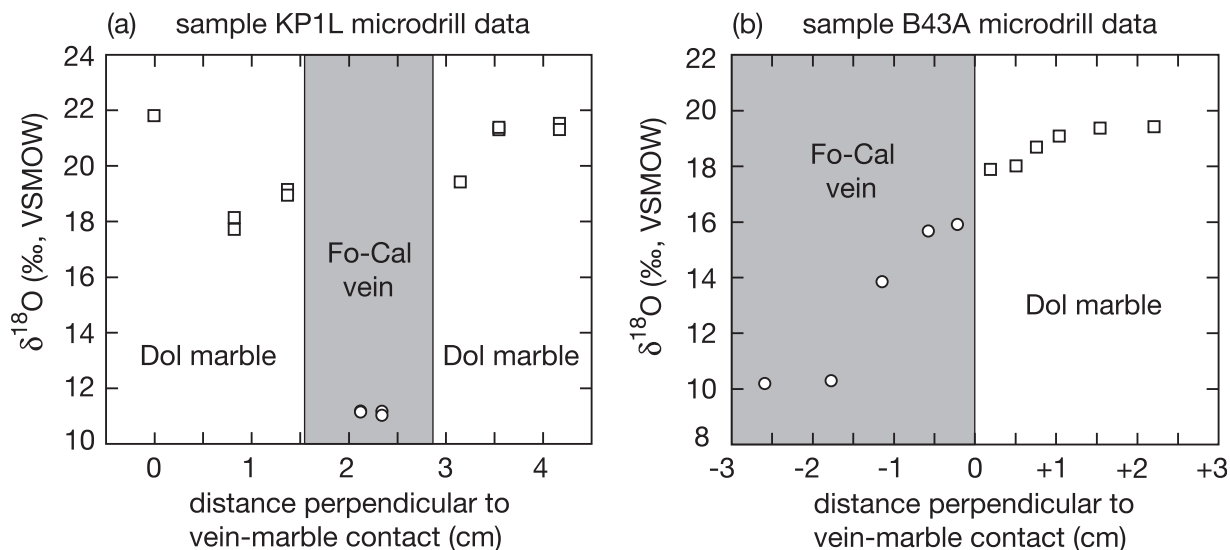
inferred T of the Fo-forming reaction (595°C). The large variation in $\delta^{18}O(Dol)$, however, precludes oxygen isotope equilibrium between Dol and either Fo or Cal. The large 10–11‰ difference between $\delta^{18}O(Fo)$ and $\delta^{18}O(Dol)$ away from the vein–marble contact (Figs 6a and 7a) indicates that $\delta^{18}O(Fo)$ was controlled by isotope exchange with low-$\delta^{18}O$ infiltrating fluid rather than with Dol.

Oxygen isotope analyses in sample B4L were conducted in areas of matrix, like that in Fig. 3c. Dolomite is uniform in $\delta^{18}O$ within error of measurement with the exception of a single outlier (Fig. 7b). Forsterite is uniform in $\delta^{18}O$ within error of measurement, and Cal is uniform with the exception of a single outlier that is suspect because it lies along a crack (Fig. 7b). The measured Dol–Cal and Cal–Fo isotope fractionations are inconsistent with equilibrium. The weighted mean $\delta^{18}O(Cal)$ is not the same as that of $\delta^{18}O(Dol)$ at a 95% confidence level, and the weighted mean $\delta^{18}O(Cal)$ exceeds that of $\delta^{18}O(Dol)$ (Fig. 7b). The equilibrium value of $\Delta^{18}O(Dol–Cal)$ at the inferred T of the Fo-forming reaction (680°C) should be $\sim$0 or slightly positive (Chacko *et al.*, 2001). The measured $\Delta^{18}O(Cal–Fo)$, 2·6 ± 0·3‰, is less than the equilibrium fractionation of 3·6‰ at 680°C (Table 3). At equilibrium, $\Delta^{18}O(Cal–Fo) = 2·6 ± 0·3‰$ would correspond to $T = 850 ± 60–70°C$, greater than the thermal stability of Dol, $\sim$740°C at the inferred P of contact metamorphism (Ferry *et al.*, 2002). The small $\sim$2–3‰ difference between $\delta^{18}O(Fo)$ and $\delta^{18}O(Dol)$ (Fig. 7b, Table 3) indicates that $\delta^{18}O(Fo)$ was controlled by isotope exchange with reactant Dol rather than with a low-$\delta^{18}O$ infiltrating fluid.

Analyses of Fo, Cal, and Dol in sample B43A were all made within $\sim$5 mm of the contact between Dol and Fo–Cal marbles (Fig. 6b). Interpretation of oxygen isotope compositions in sample B43A is complicated by a thin zone of turbid Cal along the contact in which Cal is filled with a myriad of open pores and Dol exsolution blebs and in which Fo has been extensively serpentinized (Ferry *et al.*, 2010, fig. 13a). Turbid Cal exhibits a large range in $\delta^{18}O$, 3–16‰ (Fig. 7c), that is explained by retrograde alteration, probably involving a component of meteoric water (Ferry *et al.*, 2010; see also Bowman *et al.*, 2009). Measured $\delta^{18}O$ of Dol is uniform within error of measurement (Fig. 7c, Table 3). Even ignoring analyses of turbid Cal, $\delta^{18}O$ of Cal in the Fo-Cal marble exhibits significant variation, 15·9–18·2‰ (Fig. 7c, Table 3). The measured

Fig. 6. Profiles in $\delta^{18}O$ of Cal (circles) and Dol (squares) across the contact between two Fo–Cal veins and Dol marble. Uncertainties are approximately the size of the symbols. (a) Sample KP1L from the Twin Lakes pendant. Data collected by conventional analysis at the millimeter scale as part of this study. Duplicate analyses were made at each of the eight microdrilling sites (some analyses superimpose at the scale of the diagram). (b) Sample B43A from the Beinn an Dubhaich aureole. Data are from Wing *et al.* (2000).

variation in $\delta^{18}O$ in Fo, 12·1–15·0‰, is larger (Fig. 7c). The variations in $\delta^{18}O(Cal)$ and $\delta^{18}O(Fo)$ preclude oxygen isotope equilibrium between Fo and Cal and between Dol and either mineral. The small ~2–5‰ difference between $\delta^{18}O(Fo)$ and $\delta^{18}O(Dol)$ (Fig. 7c) indicates that $\delta^{18}O(Fo)$ was controlled by isotope exchange with reactant Dol rather than with a low-$\delta^{18}O$ infiltrating fluid.

Measured $\delta^{18}O(Dol)$ in sample B1W is nearly uniform with two outliers (Fig. 7d). Values of $\delta^{18}O(Cal)$ exhibit a range of 1·6‰. The variation in $\delta^{18}O(Fo)$, 9·8–17·2‰ (Fig. 7d, Table 3), is greater than in any of the other analyzed samples. In addition, one Fo grain exhibits a core-to-rim decrease in $\delta^{18}O(Fo)$ from 12·9‰ to 9·8‰ (Fig. 7c). Non-equilibrium reverse Dol–Cal fractionations are observed [measured $\Delta^{18}O(Dol–Cal) < 0$ for some Dol–Cal pairs]. The significant variation in $\delta^{18}O(Cal)$ and $\delta^{18}O(Fo)$ precludes oxygen isotope equilibrium between Fo and Cal and between Dol and either mineral. Some Fo grains have $\delta^{18}O$ values that are only ~1–2‰ less than $\delta^{18}O(Dol)$, indicating control of $\delta^{18}O(Fo)$ by isotope exchange with reactant Dol (Fig. 7d). Other Fo grains have $\delta^{18}O$ as low as ~10‰, indicating control by isotope exchange with a low-$\delta^{18}O$ infiltrating fluid. The decrease in $\delta^{18}O$ from core to rim in one grain (Fig. 5c) is evidence for a transition during Fo growth from dolomite to fluid control of $\delta^{18}O(Fo)$.

FORMATION OF FORSTERITE BY SILICIFICATION OF DOLOMITE

Sample KP1L exhibits the best evidence that Fo formed by silicification of Dol marble according to reaction (3) with an infiltrating fluid as the source of SiO_2. First, forsterite developed in a vein-like structure that contains minor amounts of Dol. The vein is in sharp contact with Dol marble that is devoid of silicate minerals and has only traces of Cal (Table 1). The molar Ca/Mg of the Fo–Cal vein (calculated from modes and mineral compositions) and the dolomite marble are the same within error of measurement, 1·05 (Table 1). If Fo + Cal formed isochemically from a Qtz-bearing Dol protolith, the protolith must have had a molar Dol:Qtz ratio of almost exactly 2:1 with Qtz distributed in the same geometry as the vein but nowhere else in the rock. Such a combination of coincidences seems implausible. Second, the same scalloped texture at the contact between vein and Dol marble (Fig. 2a) is observed at the margins of Fo–Cal veins in Dol marble from the Bergell contact aureole. The Fo–Cal veins in the Bergell aureole have been explained by infiltration of Dol marble by Si-bearing fluids (Bucher-Nurminen, 1981; Bucher, 1998; Begue, 2008). Third, the 10–11‰ difference between $\delta^{18}O(Cal)$ in the vein and $\delta^{18}O(Dol)$ in adjacent marble (Fig. 6a) proves that the vein in sample KP1L was infiltrated by a chemically reactive, low-$\delta^{18}O$ fluid because metamorphic decarbonation reactions normally lower $\delta^{18}O$ by no more than 2–3‰ (Valley, 1986).

The veinlets in sample B4L (Fig. 3a and b) have the same mineralogy and texture as the macroscopic vein in sample KP1L, and they are assumed to have formed by the same process. Unlike sample KP1L, however, matrix between the veinlets is composed Fo + Cal + Dol rather than Dol alone. If Fo formed in the matrix by isochemical reaction(s) in a Qtz-bearing dolomite protolith, the
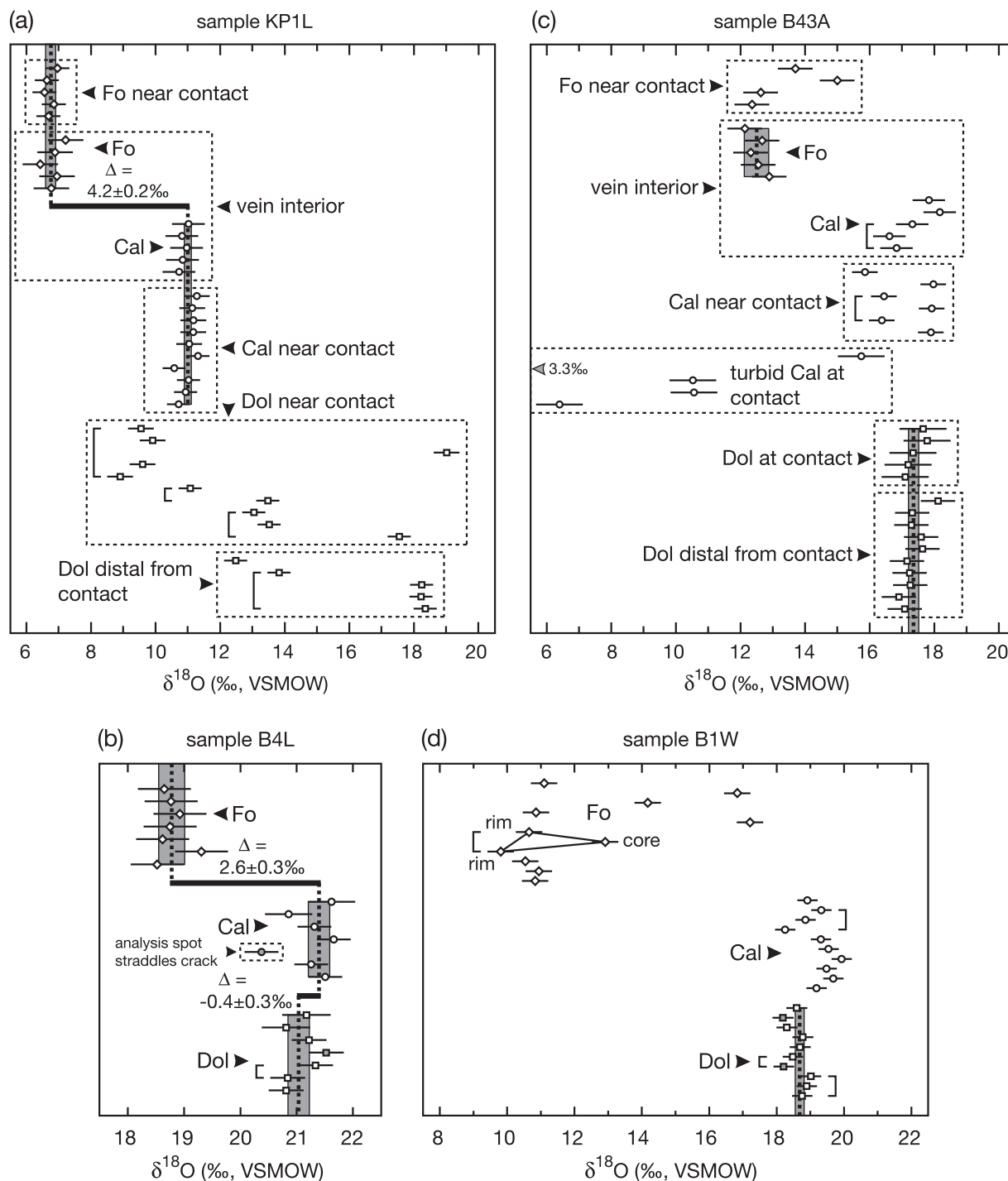
Fig. 7. Ion microprobe measurements of $\delta^{18}O$ of Cal (circles), Dol (squares), and Fo (diamonds) in samples KP1L, B4L, B43A, and B1W. Each symbol corresponds to a single analysis, and the horizontal line through the symbol represents the ± 2 SD analytical uncertainty. For groups of analyses in a sample that are statistically consistent with a uniform value at a 95% level of confidence, as indicated by the mean square weighted deviate (MSWD, Mahon, 1996), a weighted mean was computed and represented as the thick vertical dashed line. The gray band is the 95% confidence interval of the weighted mean, calculated following Mahon (1996). When all but one or two analyses in a sample or area of analysis are consistent with a uniform value, the outliers are identified by a symbol with gray shading. The outlying analyses were not used in the calculation of the weighted mean. Analyses of the same grain are grouped within square half-brackets. Thick horizontal bars and number values are either $\Delta^{18}O$(Cal–Fo) or $\Delta^{18}O$(Dol–Cal) based on the weighted mean $\delta^{18}O$ for each mineral in the sample or area of analysis. (a) Sample KP1L. Sites of most of the Cal, Dol, and Fo analyses 'near contact' are imaged in Fig. 2a. (b) Sample B4L. The single analysis of Cal along a crack is considered spurious. Analyses obtained from areas of matrix like that imaged in Fig. 3c. (c) Sample B43A. Sites of Cal and Fo analyses in the 'vein interior' are imaged in Fig. 4. (d) Sample B1W. Half the sites of Cal, Dol, and Fo analyses are imaged in Fig. 5b. The three analyses of the same Fo grain in Fig. 5c are connected with continuous lines.

amount of Fo now present (17·6 modal %) requires that the protolith contained 8·0% Qtz. This seems unlikely because dolomite and dolomitic limestone at the lowest grade in the Beinn an Dubhaich aureole, where Tlc, Tr, Di, and Fo are absent, contain <1% Qtz (Holness, 1990). More plausibly, Si was transported along grain boundaries or microfractures from veinlets into the matrix, causing limited development of Fo + Cal from Dol.

Sample B43A is interpreted to be a portion of a Fo–Cal vein in a matrix of Dol marble like the one in sample K1PL. As in sample KP1L, the Dol marble is devoid of silicate minerals and contains only a trace of Cal (Table 1). The Fo–Cal vein contains little Dol. The molar Ca/Mg of vein and Dol marble are the same within error of measurement (Table 1). The vein–marble contact has the same scalloped texture as the contact in sample KP1L. Similar to sample KP1L, measured $\delta^{18}O(Cal)$ in the vein away from its contact with Dol marble is 8–9‰ lower than $\delta^{18}O(Dol)$ away from the contact (Fig. 6b). Forsterite in sample B43A therefore almost certainly formed by the same process as did Fo in sample KP1L. The only difference is that the drill core failed to penetrate a second vein–marble contact in sample B43A.

The anastomosing Fo–Cal segregations in sample B1W (Fig. 5) have nearly the same mineralogy, occurrence, and texture as the macroscopic vein in sample KP1L. There is only a trace of Cal in the Dol matrix of sample B1W, and the Fo–Cal segregations contain only ∼1% Dol (Table 1). The estimated Ca/Mg of the segregations is the same within error of measurement as Ca/Mg of matrix Dol

(Table 1). The scalloped texture of the contact between Fo–Cal segregations and Dol matrix in sample B1W is the same as along the vein–marble contact in sample KP1L. Forsterite in the segregations therefore presumably formed by the same process of silica metasomatism as in sample KP1L. The only difference is that the vein in sample KP1L is approximately planar and the segregations in sample B1W are not.

Estimates of the T at which Fo formed in samples B43A and B1W are independent evidence that Fo did not form by isochemical reactions (1) or (2). The T recorded by Cal inclusions in Fo in samples B1W and B43A (Table 2) is at least 130–165°C above the thermal stability of Di + Dol + Fo + Cal and Tr + Dol + Fo + Cal in equilibrium with CO_2–H_2O fluid at 500 bars (Ferry et al., 2002, fig. 7). The estimated temperatures are too high for Fo to have formed by isochemical reactions (1) or (2) unless they were significantly overstepped.

PHASE EQUILIBRIA, REACTION PATHS, AND TIME-INTEGRATED FLUID FLUX

Phase equilibria and mineral–fluid reactions

Formation of Fo by reaction (3) with aqueous silica [$SiO_2(aq)$] as the source of SiO_2 is controlled by the activities of SiO_2 and CO_2, a_{SiO_2} and a_{CO_2}, as well as by T and P. Figure 8 illustrates the control of a_{SiO_2} and a_{CO_2}
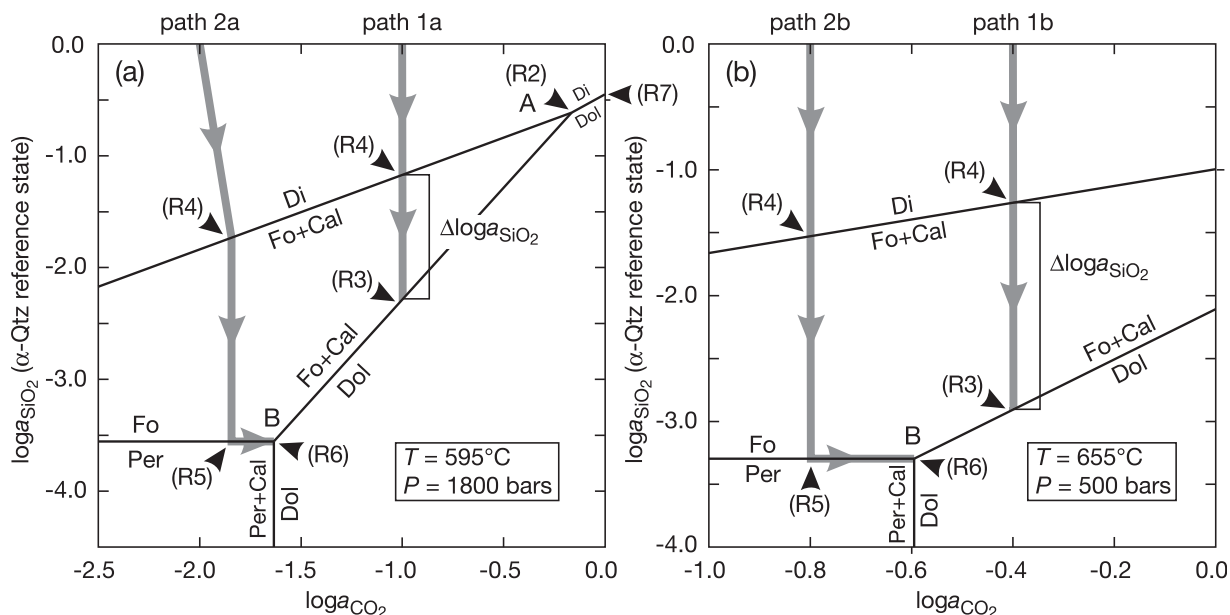

Fig. 8. Stability of combinations of Fo, Dol, Cal, Di, and Per as a function of a_{CO_2} and a_{SiO_2} at P–T conditions relevant to the formation of Fo by silicification in samples KP1L (a) and B43A (b). The reference state for a_{SiO_2} is unit activity defined by equilibrium with α-Qtz. Reactions (2)–(7) are the same as those in the text. Thick gray lines define the trajectory of fluid composition during infiltration of dolomite by Qtz-saturated H_2O–CO_2 fluid (log a_{SiO_2} = 0); arrowheads point in the direction of flow.

for P–T conditions appropriate to formation of Fo in sample KP1L (Fig. 8a) and in sample B43A (Fig. 8b). The diagrams have almost the same topology. The difference is that reaction (2) is stable at P–T conditions of Fig. 8a (shown as isothermal, isobaric invariant point A). At 500 bars (Fig. 8b) 655°C lies above the thermal maximum of reaction (2).

Formation of Fo by reaction (3) occurs over a restricted range of both a_{SiO_2} and a_{CO_2}. At conditions of Fig. 8a, $\log a_{CO_2}$ must lie between -0.162 of the Di–Dol–Fo–Cal invariant point (A) and -1.632 of the Dol–Per–Cal–Fo invariant point (B), and $\log a_{SiO_2}$ correspondingly must lie between -0.619 and -3.560. At conditions of Fig. 8b, the corresponding limits on $\log a_{CO_2}$ and $\log a_{SiO_2}$ are 0 to -0.594 and -2.113 to -3.301, respectively. The products of reaction (3), Fo and Cal, as well as reactant Dol, likewise are stable only over limited ranges of $\log a_{CO_2}$ and $\log a_{SiO_2}$. At a_{CO_2} less than that of the Di–Dol–Fo–Cal invariant point A (where stable; $a_{CO_2} = 1$ otherwise) and at values of a_{SiO_2} higher than the Di–Fo–Cal equilibrium, Fo + Cal reacts to Di by

$$Fo + 2\ Cal + 3\ SiO_2(aq) = 2\ Di + 2\ CO_2. \qquad (4)$$
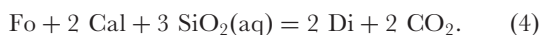
At a_{CO_2} between the Di–Dol–Fo–Cal invariant point A (if stable; $a_{CO_2} = 1$ otherwise) and the Dol–Per–Cal–Fo invariant point B and at values of a_{SiO_2} less than the Dol–Fo–Cal equilibrium, Fo + Cal reacts to Dol by the reverse of reaction (3). At a_{CO_2} less than the Dol–Per–Cal–Fo invariant point and at a_{SiO_2} less than the Fo–Per equilibrium, Fo reacts to Per (MgO) by

$$Fo = 2\ Per + SiO_2(aq) \qquad (5)$$
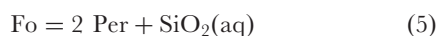
and Dol reacts to Per + Cal by

$$Dol = Per + Cal + CO_2. \qquad (6)$$

At a_{CO_2} above the Di–Dol–Fo–Cal invariant point A (if stable) and at higher a_{SiO_2} than the Di–Dol equilibrium, Dol reacts to Di by

$$Dol + 2\ SiO_2(aq) = Di + 2\ CO_2. \qquad (7)$$

Fluid speciation and reaction paths

Reactive fluids that drive mineral reactions and oxygen isotope alteration during contact metamorphism of carbonate rocks are believed in most cases to be of magmatic origin (e.g. review of Ferry *et al.*, 2002). Magmatic fluids should be at or close to Qtz saturation ($a_{SiO_2} = 1$). When Qtz-saturated H_2O–CO_2–SiO_2 fluid infiltrates dolomite, a series of mineral reaction fronts develop along the flow path. These reactions and the conditions at which they occur can be predicted from Fig. 8 and the model for Si speciation in H_2O–CO_2–SiO_2 fluids of Newton & Manning (2009).

Fluid speciation

Laboratory measurements of the molality of SiO_2 in Qtz-saturated H_2O–CO_2 fluids over the range $X_{H_2O} = 0.25 - 1$ and in H_2O fluids over the range of a_{SiO_2} between those defined by the Qtz and forsterite–rutile–geikielite buffers are accurately reproduced by considering ideal mixing of just two Si species in the fluid, a monomer (m), $Si(OH)_4·2H_2O$, and a dimer (d), $Si_2(OH)_6·4H_2O$ (Newton & Manning, 2009). Mole fractions of the two species in H_2O–CO_2–SiO_2 fluid are related by the equilibrium constant, K_{md}:

$$K_{md} = [(X_d)(a_{H_2O})]/(X_m)^2 \qquad (8)$$

with K_{md} computed from

$$\log K_{md} = 1.480 + 0.0012\,T(K) \\ + (0.000119\,T - 0.165)P(kbar) \qquad (9)$$

(Newton & Manning, 2009). The mole fraction of total dissolved aqueous silica in the fluid is

$$X_{SiO_2(aq)} = X_m + 2\ X_d. \qquad (10)$$

At specified P and T, values of X_d* and X_m* at $a_{SiO_2} = a_{H_2O} = 1$ were computed from equations (8)–(10), and the expression for Qtz solubility in H_2O fluids of Fournier & Potter (1982). Given the very small values of $X_{SiO_2(aq)}$, fluid may be approximated as a CO_2–H_2O solution for the purposes of relating a_{H_2O}, a_{CO_2}, X_{H_2O}, and X_{CO_2} through an EOS for CO_2–H_2O fluid (Newton & Manning, 2009). The EOS used in this study is that of Kerrick & Jacobs (1981). For any combination of reduced a_{SiO_2} and a_{H_2O},

$$X_m = (X_m*)(a_{SiO_2})(a_{H_2O})^4 \qquad (11)$$

$$X_d = (X_d*)(a_{SiO_2})^2(a_{H_2O})^7 \qquad (12)$$

and the value of $X_{SiO_2(aq)}$ is calculated from equation (10).

Reaction paths

Infiltration of dolomite by Qtz-saturated H_2O–CO_2–SiO_2 fluid produces a sequence of mineral assemblages along the flow path that depend on a_{CO_2} of the input fluid, $a^\circ_{CO_2}$. At P–T conditions at which reaction (2) is stable, fluid with relatively large $a^\circ_{CO_2}$ will simply convert Dol to Di by reaction (7) along a sharp reaction front (Fig. 8a). Quartz-saturated CO_2-rich fluids, however, are unlikely during contact metamorphism, and this possibility is not considered further. Forsterite is produced from Dol by reaction (3) if fluid has intermediate $\log a^\circ_{CO_2}$, such -1.0 and -0.4 in Fig. 8a and b. Gray lines 1a and 1b illustrate the sequence of minerals, mineral reactions, and values of $\log a_{CO_2}$ and $\log a_{SiO_2}$ along the flow path (arrowheads point in the direction of flow). Dolomite is stable distal to the inlet to the flow system. As the inlet is approached

from Dol, a sharp reaction front is first encountered that separates unreacted Dol downstream from Fo + Cal rock upstream. The reaction front is defined by the complete conversion of Dol to Fo + Cal by reaction (3). Closer to the inlet, the flow system is composed of Fo + Cal until a second reaction front is encountered that separates Fo + Cal downstream from Di upstream. The second reaction front is defined by the complete conversion of Fo + Cal to Di by reaction (4). Between the second reaction front and the inlet, the flow system is composed of only Di that is in equilibrium with the input Qtz-saturated fluid. Fluid coexisting with Fo + Cal between the two reaction fronts has composition in equilibrium with Di + Fo + Cal at the upstream reaction front. Fluid coexisting with Dol downstream from the distal reaction front has composition in equilibrium with Dol + Fo + Cal at the distal front. The changes in fluid composition across the Di–Fo–Cal and Dol–Fo–Cal reaction fronts are illustrated in Fig. 8 by the trajectories of paths 1a and 1b across the Di and Fo + Cal stability fields, respectively.

For input fluid with a given $\log a^{\circ}_{CO_2}$, the reaction path can be computed. Fluid with $\log a^{\circ}_{CO_2} = -1 \cdot 0$ in Fig. 8a is an example. First, X_d^* and X_m^* were calculated for 595°C and 1800 bars. Second, $X^{\circ}_{CO_2}$, $X^{\circ}_{H_2O}$, and $a^{\circ}_{H_2O}$ were computed from $a^{\circ}_{CO_2}$ using the EOS for CO_2–H_2O fluid. Third, X_m, X_d, and $X_{SiO_2(aq)}$ of the input fluid, X_m°, X_d°, and $X^{\circ}_{SiO_2(aq)}$, were calculated from equations (10)–(12). Because the reaction path is almost vertical in Fig. 8, X_m, X_d, and $X_{SiO_2(aq)}$ at the Di–Fo–Cal reaction front were initially computed assuming no change in a_{CO_2} but decreasing a_{SiO_2} to that of the Di–Fo–Cal equilibrium at $\log a^{\circ}_{CO_2} = -1 \cdot 0$. The decrease in X_m, X_d, and $X_{SiO_2(aq)}$ at the reaction front $[\Delta X_m, \Delta X_d,$ and $\Delta X_{SiO_2(aq)}]$ is the difference between X°_m, X°_d, and $X^{\circ}_{SiO_2(aq)}$ and X_m, X_d, and $X_{SiO_2(aq)}$ of fluid equilibrated with Di + Fo + Cal. For every mole input fluid, $(2/3)[\Delta X_{SiO_2(aq)}]$ moles CO_2 and $(4\Delta X_m + 7\Delta X_d)$ moles H_2O are added to the fluid at the reaction front. The estimate of the equilibrium values of X_{CO_2} and a_{CO_2} at the Di–Fo–Cal reaction front were then updated and the calculation repeated until no significant further change in a_{CO_2} occurred. Finally, X_m, X_d, and $X_{SiO_2(aq)}$ at the Dol–Fo–Cal reaction front were computed similarly taking the value of a_{CO_2} at the Di–Fol–Cal reaction front as the initial estimate of a_{CO_2} at the Dol–Fo–Cal reaction front. The slopes of calculated paths 1a and 1b in Fig. 8 are negative and positive, respectively. The deviation from vertical is imperceptible at the scale of the figure because $\Delta X_{SiO_2(aq)}$ at the two reaction fronts is very small relative to X_{CO_2}.

In anticipation of discussion of the role of silicification in the formation of Per during contact metamorphism of dolomite, reaction paths were also considered for values of $a^{\circ}_{CO_2}$ less than that of the Dol–Per–Cal equilibrium (paths 2a and 2b, Fig. 8). In both cases, Dol is stable distal from

the inlet to the flow system. As the inlet is approached from Dol, a sharp reaction front is encountered that separates unreacted Dol downstream from rock upstream composed of Per + Cal with a minute quantity of Fo. The reaction front is defined by the complete conversion of Dol to Per + Cal by reaction (6) [with the minute quantity of Fo produced by reaction (3)]. Closer to the inlet, the flow system is composed of Per + Cal + trace Fo until a second reaction front is encountered that separates Per + Cal + trace Fo downstream from Fo + Cal upstream. The second reaction front is defined by the complete conversion of Per to Fo by the reverse of reaction (5). Closer yet to the inlet, the flow system is composed of Fo + Cal until a third reaction front is encountered that separates Fo + Cal downstream from Di upstream. The third reaction front is defined by the complete conversion of Fo + Cal to Di by reaction (4). Between the Di–Fo–Cal reaction front and the inlet, the flow system is composed only of Di that is in equilibrium with the input Qtz-saturated fluid. Fluid coexisting with Fo + Cal rock between the Di–Fo–Cal and the Fo–Per reaction fronts has composition in equilibrium with Di + Fo + Cal at the reaction front upstream. Fluid coexisting with Per–Cal–Fo rock between the Fo–Per and the Dol–Per–Cal–Fo reaction fronts has composition in equilibrium with Fo + Per + Cal at the reaction front upstream. Fluid coexisting with Dol downstream from the distal Dol–Per–Cal–Fo reaction front has composition of the Dol–Per–Cal–Fo invariant point (B). The change in fluid composition across the Di–Fo–Cal and Fo–Per reaction fronts is illustrated in Fig. 8 by the trajectories of paths 2a and 2b across the Di and Fo + Cal stability fields, respectively. The change in fluid composition across the Dol–Per–Cal–Fo reaction front involves an increase in a_{CO_2} at constant a_{SiO_2}, and is illustrated by the portions of paths 2a and 2b that follow the Fo–Per equilibrium curve to the Dol–Per–Cal–Fo invariant point.

Fluid compositions along paths 2a and 2b were computed in a manner similar to computations of fluid composition along paths 1a and 1b. Path 2a is an example. Values of a_{CO_2}, a_{SiO_2}, X_m, X_d, and $X_{SiO_2(aq)}$ at the Di–Fo–Cal reaction front were computed in exactly the same way as along path 1a with the exception that $a^{\circ}_{CO_2}$ is 0·01 rather than 0·1. The portion of path 2a through the Di stability field in Fig. 8a has a discernible negative slope because a_{CO_2} is sufficiently low that X_{CO_2} is comparable with $\Delta X_{SiO_2(aq)}$ at the reaction front. Values of X_m, X_d, and $X_{SiO_2(aq)}$ at the Fo–Per reaction front were easily computed because reaction (5) negligibly changes X_{H_2O}. The value of a_{CO_2} at the Fo–Per reaction front therefore is almost identical to a_{CO_2} at the Di–Fo–Cal reaction front upstream, and path 2a is almost vertical through the Fo + Cal stability field in Fig. 8a. Values of a_{CO_2}, a_{SiO_2}, X_m, X_d, and $X_{SiO_2(aq)}$ at the Per–Cal–Fo–Dol reaction

front were computed exactly because a_{CO_2} and a_{SiO_2} at the reaction front are those defined by the Dol–Per–Cal–Fo invariant point (B). The minute quantity of Fo produced by reaction (3) at the Dol–Per–Cal–Fo reaction front results from the small decrease in $X_{SiO_2(aq)}$, caused by the increase in a_{CO_2} at constant a_{SiO_2}, along the flow path between the Fo–Per and Per–Cal–Fo–Dol reaction fronts (Fig. 8). Specifically in the case of path 2a, 7×10^{-9} mole Fo is produced per mole infiltrating fluid at the Dol–Per–Cal–Fo reaction front, corresponding to 2×10^{-4} modal % Fo in the resulting Per–Cal–Fo rock.

Time-integrated fluid flux and model fluid flow columns

Time-integrated fluid flux

The molar time-integrated fluid flux (q_m in units of mol fluid cm^{-2} rock) associated with formation of Fo by silicification of Dol can be computed for a given $a^\circ_{CO_2}$ of the input fluid. Because the spatial scale over which Fo develops by silicification of Dol is not accurately known, calculated values of q_m are normalized to the development

of 1 cm^3 Fo–Cal rock along the fluid flow path. The conversion of Dol to 1 cm^3 Fo + Cal rock requires progress of reaction (3), ξ_3, of 8.51×10^{-3} in mole units. Along path 1a (Fig. 8a), as an example, log $a^\circ_{CO_2} = -1.0$, and $\Delta X_{SiO_2(aq)}$ at the Dol–Fo–Cal reaction site is 9.07×10^{-5}. Because $\Delta X_{SiO_2(aq)}$ is small, to an excellent approximation,

$$q_m = \xi_3/\Delta X_{SiO_2(aq)} = (8.51 \times 10^{-3})/(9.07 \times 10^{-5})$$
$$= 94 \text{ mol fluid } cm^{-2} rock \cdot cm^{-1} \text{ flow path.} \quad (13)$$

Development of even 1000 cm of Fo + Cal rock per 1 cm^2 area of rock perpendicular to the flow path therefore requires $q_m \approx 10^5$ mol fluid cm^{-2} rock, 1–2 orders of magnitude more than is involved in mineral reactions driven by pervasive reactive fluid flow in most contact aureoles (Ferry *et al.*, 2002, table 17). Figure 9 illustrates how calculated values of q_m vary with $a^\circ_{CO_2}$ of the input fluid at *P–T* conditions specific for Fig. 8a. Unless log $a^\circ_{CO_2}$ is high (>-0.4), calculated values of q_m do not vary by more than a factor of 2–3. At elevated values of $a^\circ_{CO_2}$, calculated q_m becomes very large, rising to infinity at $a^\circ_{CO_2}$ corresponding to the Di–Dol–Fo–Cal invariant point A of Fig. 8a
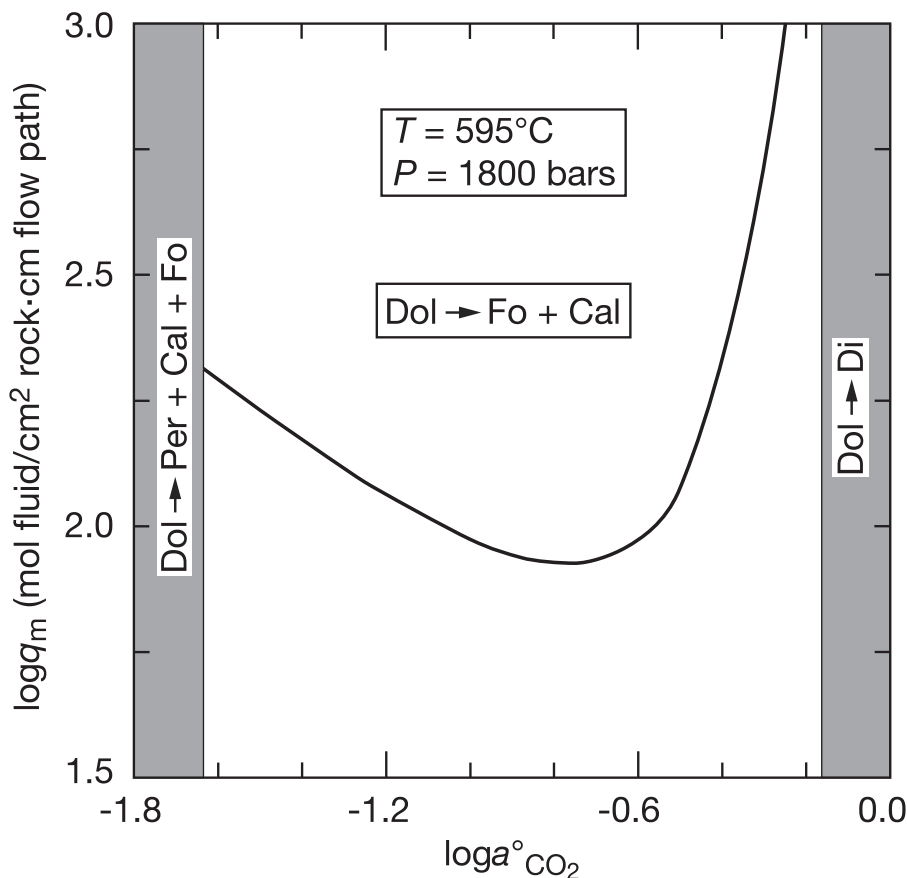

Fig. 9. Calculated time-integrated fluid flux (q_m) needed to form 1 cm^3 Fo + Cal from Dol as a function of $a^\circ_{CO_2}$ along fluid flow paths like 1a in Fig. 8a. Formation of Fo + Cal from Dol is limited to log $a^\circ_{CO_2}$ less than −0·162 (Dol reacts to Di at larger values) and greater than −1·632 (Dol reacts to Per + Cal + Fo at smaller values).

(where $\Delta X_{SiO_2(aq)} = 0$). For comparison between the Twin Lakes pendant and the Beinn an Dubhaich aureole, q_m for conversion of Dol to $1\,cm^3$ Fo + Cal by reaction (3) along path 1b (Fig. 8b) is even larger, $1\cdot2 \times 10^3\,mol$ fluid cm^{-2} rock·cm^{-1} flow path. The larger value is explained by the decrease in the silica content of fluid with increasing X_{CO_2} and hence decreasing a_{H_2O} [equations (11) and (12)].

Model fluid flow columns

Values of q_m at the other reaction fronts along the different flow paths in Fig. 8 can be calculated in an analogous fashion. This leads to predictions of the spatial distributions of mineral assemblages along the path. Fluid flow will produce an oxygen isotope alteration front as well as mineral reaction fronts because infiltrating fluid in contact aureoles normally is pluton-derived with $\delta^{18}O$ 10–20‰ less than for unaltered marine carbonate rocks. The displacement (z) of the oxygen isotope front from the inlet to the flow system can be integrated with the spatial distribution of mineral assemblages by

$$z = q_m(N_f/V_r) \qquad (14)$$

where N_f is the number of moles oxygen per mole fluid and V_r is the number of moles oxygen per unit volume of rock (Dipple & Ferry, 1992). The model flow column associated with path 1a, Fig. 8a, is an example. Along the flow path $q_m = 94\,mol\,cm^{-2}$ rock is required to form $1\,cm^3$ Fo + Cal from Dol by reaction (3) along the direction of flow [equation (13)]. The q_m required to form $1\,cm^3$ Di from Fo + Cal by reaction (4), calculated similarly, is $9\cdot6\,mol\,cm^{-2}$. Because fluid in the flow system has $X_{CO_2} \approx 0\cdot0527$ and oxygen isotope alteration occurs exclusively in Dol, $N_f = 1\cdot0527$ and $V_r = 0\cdot0933\,mol$ oxygen cm^{-3} rock. The oxygen isotope alteration front is displaced $1\,cm$ downstream for every increment of $q_m = 0\cdot0887\,mol$ fluid cm^{-2} rock [equation (14)]. The calculated spatial distribution of mineral assemblages and isotope alteration along flow path 1a, referenced to unit length of Di ($L_{Di} = 1$), is listed in Table 4. Proceeding downstream, Fo + Cal develops over a distance $0\cdot102L_{Di}$. Oxygen isotope alteration occurs over a distance $108L_{Di}$ and includes altered Di, Fo + Cal, and a large distance of Dol ($106\cdot9L_{Di}$) downstream from Fo + Cal.

Spatial distributions of mineral assemblages and isotope alteration along paths 2a and 2b were computed similarly to those along paths 1a and 1b (Table 4). The principal difference between paths 1a and 2a is the development of Per + Cal from Dol. The value of q_m required to produce $1\,cm^3$ Per + Cal along the flow path from Dol by reaction (6) is

$$q_m = \xi_6[1 - X_{CO_2}(DPC)]/[X_{CO_2}(DPC) - X^\circ_{CO_2}] \quad (15)$$

where ξ_6 is progress of reaction (6) that converts Dol to $1\,cm^3$ Per + Cal, $X_{CO_2}(DPC)$ is the mole fraction of CO_2

Table 4: Predicted spatial distribution of mineral assemblages and oxygen isotope alteration in model flow systems

Path	Di	Fo + Cal	Per + Cal	Oxygen isotope alteration
1a	1	$1\cdot02 \times 10^{-1}$		$1\cdot08 \times 10^2$
1b	1	$1\cdot28 \times 10^{-1}$		$2\cdot22 \times 10^3$
2a	1	$2\cdot62 \times 10^{-2}$	$1\cdot47$	$7\cdot93 \times 10^1$
2b	1	$5\cdot54 \times 10^{-2}$	$1\cdot96 \times 10^2$	$4\cdot29 \times 10^2$

Values are distances along the flow path normalized to unit distance of Di developed at the inlet to the flow system.

in fluid in equilibrium with Dol + Per + Cal, and $X^\circ_{CO_2}$ refers to fluid downstream from the Di–Fo–Cal reaction front (Ferry & Rumble, 1997). Results appear in Table 4.

The predicted spatial scale of oxygen isotope alteration along all paths is much greater than the scale of mineral reaction because the oxygen content of fluid is significantly greater than either the carbon or silica content of the fluid. The predicted scale of decarbonation reaction (6) is significantly greater than the scale of silicification reactions (3)–(5) along paths 2a and 2b because the fluid contains much more dissolved carbon than dissolved silica. The predicted distance over which Fo + Cal develops by reaction (3) is much smaller than the distance over which Di develops because reaction (4) strips ~96% of the dissolved silica from the input fluid leaving little for silicification of Dol further downstream (Fig. 8). The predicted scale of oxygen isotope alteration relative to the scale of silicification is larger along paths 1b and 2b, compared with paths 1a and 2a, because fluids along paths 1b and 2b have larger X_{CO_2} and hence lower a_{H_2O} and lower concentrations of dissolved silica [equations (11) and (12)].

DISCUSSION
Formation of forsterite over a range of reaction affinity
Empirical evidence for a range of reaction affinity

A departure from equilibrium (positive reaction affinity, A, with units of cal) is required to drive all chemical reactions. Measured Fo crystal number densities in samples KP1L, B4L, B43A, and B1W (Table 3) indicate that reaction affinity was variable during formation of Fo by reaction (3). The ratio of crystal nucleation rate to crystal growth rate, NR/GR, continuously and monotonically increases with increasing A (Roselle et al., 1997, fig. 5; Müller et al., 2009, fig. 13). The measured Fo crystal number density, referenced to unit volume of Fo, is

equivalent to the value of NR/GR averaged over the duration of reaction (3). Crystal number density varies by 2–3 orders of magnitude, increasing among the analyzed samples in the order KPlL, B4L, B43A, and BlW (Table 3). The NR/GR ratio, and hence A, during formation of Fo therefore increased in the same order. Because the Fo number density on a mole basis in samples B4L, B43A, and BlW is larger than in all samples analyzed by Roselle *et al.* (1997), A must have been unusually large during formation of Fo in the Beinn an Dubhaich aureole compared with the Ubehebe Peak aureole.

Cause and magnitude of variations in reaction affinity

The cause and magnitude of variations in reaction affinity during formation of Fo by reaction (3) can be explained by phase equilibria (Fig. 8). Reaction (3) is modeled as an isothermal, isobaric process. Minerals involved in the reaction are nearly pure substances (Table 2), and the change in a_{CO_2} during reaction is negligibly small (paths 1a, 1b, Fig. 8). Reaction affinity during formation of Fo therefore is $A = 2 \cdot 303 RT \Delta \log a_{SiO_2}$, where $\Delta \log a_{SiO_2}$ is the difference between $\log a_{SiO_2}$ of input fluid at the site of reaction (3) (that defined by the Di–Fo–Cal equilibrium) and $\log a_{SiO_2}$ of fluid in equilibrium with $Dol + Fo + Cal$ at the same value of a_{CO_2} (Fig. 8). Accordingly, $\Delta \log a_{SiO_2}$ at the start of reaction can vary between nearly zero near the Di–Dol–Fo–Cal invariant point, A (if stable) and ~ 2. This corresponds to values of A between ~ 0 and ~ 8500 cal specifically for sample KPlL (Fig. 8a). In cases like the samples from Beinn an Dubhaich aureole where T was above the stability of invariant point A during metamorphism, the range of A is between the value at $\log a_{CO_2} = 0$ (~ 4700 cal) and ~ 8500 cal (Fig. 8b). In comparison with a thermally overstepped reaction with a representative $\Delta \bar{S}$ of ~ 20 cal deg^{-1}mol^{-1} volatiles (Walther & Wood, 1986), the 8500 cal value corresponds to an overstep in T of $\sim 210°C$ [reaction (3) produces 2 moles CO_2]. Departures from equilibrium at the site of reaction (3) therefore can be very large, especially when input fluids have a_{CO_2} close to that defined by the Dol–Per–Cal equilibrium. Variations in A during reaction (3) can be simply explained by variation in a_{CO_2} of input fluid with values of A increasing with decreasing a_{CO_2}.

Carbon isotope data support the conclusion that reaction affinity was controlled by the CO_2 content of the infiltrating fluid. Sample KPlL records the lowest value of A of the four analyzed samples. Measured $\delta^{13}C(Cal)$ in the sample is 3–4‰ less than $\delta^{13}C(Dol)$ away from the vein–marble contact (Ferry *et al.*, 2010, fig. 3a). The difference in $\delta^{13}C$ is too large to have been produced by a decarbonation reaction that releases half the carbon in a rock as CO_2 (Ferry & Rumble, 1997). The difference between $\delta^{13}C(Cal)$ and $\delta^{13}C(Dol)$ was caused by infiltration of the vein by a relatively CO_2-rich, low-$\delta^{13}C$ fluid. In contrast, $\delta^{13}C(Cal)$ and $\delta^{13}C(Dol)$ differ on average by no more

than 0·5‰ in the other three samples that record higher values of A (Ferry *et al.*, 2010, figs 6 and 7), consistent with (but not proving) relatively CO_2-poor infiltrating fluids.

Correlations among forsterite textures and grain-scale behavior of oxygen isotopes

Observed empirical correlations

Samples KPlL, B4L, B43A, and BlW are listed Table 3 and positioned along the vertical axis of Fig. 10 in order of increasing Fo crystal number density. The average Fo crystal size correlates inversely with Fo crystal number density because average crystal size is the inverse of the cube root of number density. Crystal number density also correlates with Fo crystal morphology. Forsterite in sample KPlL, with the lowest crystal number density, has a blocky morphology (Fig. 2b). Most or all Fo in samples B43A and BlW with the highest crystal number density has a rounded, bead-like shape (Figs 4 and 5b). Forsterite in sample B4L with intermediate number density has a tabular morphology (Fig. 3c).

Forsterite crystal number density further correlates with the degree of oxygen isotope homogeneity and equilibration of the mineral products of reaction (3). In sample KPlL, with the lowest Fo crystal number density, Fo and Cal are uniform in $\delta^{18}O$ within error of measurement and have a measured $\Delta^{18}O(Cal–Fo)$ within error of the expected equilibrium value at the inferred T of reaction (3) (Figs 7a and 10; Table 3). Forsterite and Cal in sample B4L, with the next higher Fo number density, are uniform in $\delta^{18}O$, or nearly so, but the measured $\Delta^{18}O(Cal–Fo)$ is smaller than the expected equilibrium value at the inferred T of reaction (3) (Figs 7b and 10; Table 3). Samples B43A and BlW, with the highest Fo number density, contain Fo and Cal that are both inhomogeneous in $\delta^{18}O$ and, therefore, did not attain equilibrium. The range in $\delta^{18}O(Fo)$ is largest in sample BlW, which has the highest Fo number density (Figs 7d and 10; Table 3).

Causes of the observed correlations

The observed correlations among textures and oxygen isotope behavior imply the arrangement of samples along the vertical axis of Fig. 10 can be explained by increasing A from bottom to top (in turn controlled by decreasing X_{CO_2} of the infiltrating fluid). Forsterite crystal number density and average size are correlated with A because an increase in A causes an increase in the ratio NR/GR. Reaction affinity can also explain the rounded, bead-like Fo morphology in samples B43A and BlW in one or both of two different ways. First, elevated A may promote kinetic roughening that produces rounded crystal shapes (Roselle *et al.*, 1997). Second, small crystals produced at large A attain textural equilibrium faster than large crystals (Holness & Siklos, 2000). Because the equilibrium Fo–Cal–Cal dihedral angle is $\sim 165°$ (Holness *et al.*, 1991), the small Fo crystals would then adopt a
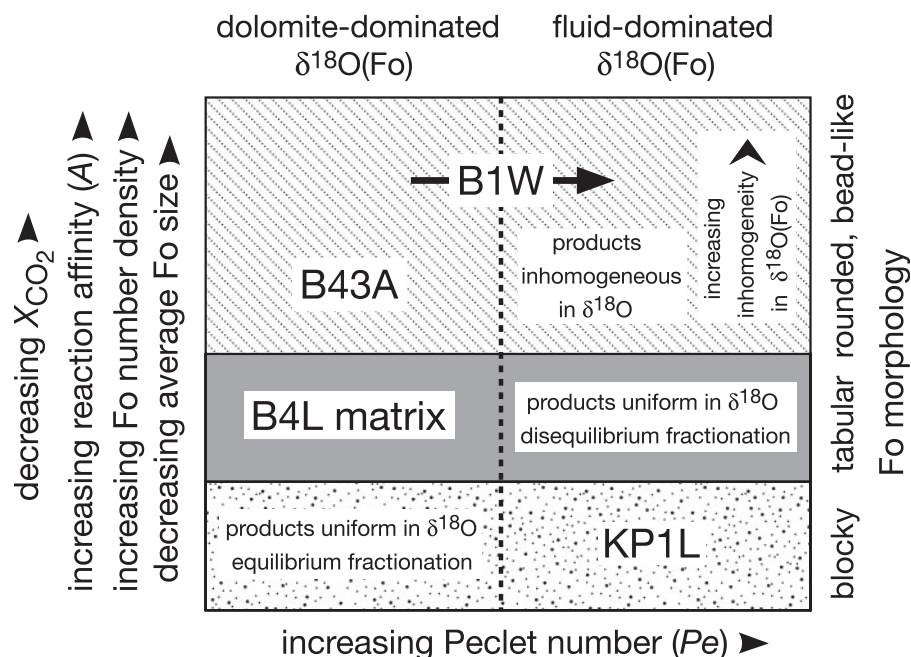
Fig. 10. Summary of correlations among the textures of Fo and the oxygen isotope systematics of Fo and Cal in the four analyzed samples. The crystal size, number density, and morphology of Fo are correlated with the degree of isotope homogeneity and equilibration of the products of reaction (3), Fo and Cal. The correlations can be explained by a range of reaction affinity, which, in turn, was controlled by a range in X_{CO_2} of the infiltrating fluid. Whether $\delta^{18}O(Fo)$ was controlled by isotope exchange with infiltrating fluid or with reactant Dol was determined by the Peclet number rather than by reaction affinity. Arrow through label for sample BlW represents the inferred transition from Dol control to fluid control of $\delta^{18}O(Fo)$ during growth of Fo.

rounded shape. The details of how lower values of A lead to the blocky and tabular Fo in samples KPlL and B4L are not known.

Reaction affinity potentially controls the degree of homogeneity and equilibration of the oxygen isotope compositions of Fo and Cal by, in turn, controlling GR/D, where D is the effective diffusivity of relevant isotopic species in the growth medium (Bickle *et al.*, 1997; Watson & Müller, 2009). Because the equilibrium $\Delta^{18}O(Cal–Fo) > 0$ and $\Delta^{18}O(Dol–Cal) \approx 0$ during metamorphism, growth of Fo by reaction (3) under conditions of high GR/D will enrich the environment immediately surrounding the Fo crystals in ^{18}O relative to ^{16}O (Watson & Müller, 2009, fig. 1). Depending on the spacing of Fo crystals and the width of the halo of elevated $\delta^{18}O$ around each crystal, variations in $\delta^{18}O$ may then develop among nearby grains of Fo as well as within single Fo grains.

The control of $\delta^{18}O(Fo)$, as represented by the arrangement of samples along the horizontal coordinate of Fig. 10, is explained by variations in factors other than A, specifically those that define the chemical Peclet number, $Pe = \mathcal{J}h/D$ (e.g. Bickle & McKenzie, 1987). Fluid flux is $\mathcal{J}$, and h is the distance between a growing Fo crystal and the nearest reactant Dol. At constant D, when $\mathcal{J}$ and/or h are large, Pe is large, and isotope transport is dominated by advection rather than by diffusion. The $\delta^{18}O$ of Fo and

Cal are expected to represent equilibrium or approach to equilibrium with the input fluid. Because the input fluid during contact metamorphism typically has much lower $\delta^{18}O$ than normal marine carbonates, measured $\delta^{18}O$ of Fo and Cal then will be significantly lower than reactant Dol. Sample KPlL (Figs 6a and 7a) is an example. When $\mathcal{J}$ and/or h are small, Pe is small, and isotope transport is dominated by diffusion. The $\delta^{18}O$ of product minerals at the site of reaction (3) is expected to represent equilibrium or approach to equilibrium with the reactant Dol. Samples B4L and B43A are examples (Fig. 7b and c). The occurrence of Fo grains with either dolomite- or fluid-dominated $\delta^{18}O$ and the observed core-to-rim decrease in $\delta^{18}O(Fo)$ in sample BlW (Figs 5c and 7d) can be explained by increasing Pe during the growth of Fo. Variations in Pe during progress of reaction (3) also can explain grain-scale variations in $\delta^{18}O(Fo)$ and $\delta^{18}O(Cal)$.

The differences between the four samples in Fo crystal number density and average size, in the degree of oxygen isotope variability and equilibration of Fo and Cal, and in whether $\delta^{18}O(Fo)$ was dominated by isotope exchange with Dol or with fluid (Fig. 10) can all be explained by variations in A and Pe during formation of Fo. Sample KPlL experienced reaction (3) at low values of A and high values of Pe. Sample B4L developed at higher A but a lower Pe. Forsterite formed in sample B43A also at low

Pe but at still higher *A*. Sample BlW experienced reaction (3) at the highest value of *A* and over a range in *Pe* that increased during Fo growth.

Redistribution of oxygen isotopes during formation of forsterite

Various models have been proposed for the redistribution of oxygen isotopes among minerals during metamorphic mineral reactions. The conventional model assumes that the redistribution occurs with isotope exchange equilibrium among all reactants and products at all times (e.g. Rumble, 1982; Chamberlain *et al.*, 1990). More recently, Müller *et al.* (2004) presented evidence that products are in oxygen isotope exchange equilibrium during reactions but that reactants and products are out of equilibrium. The measurements of δ^{18}O of Fo, Cal, and Dol in samples KPlL, BlW, B4L, and B43A provide a direct test of which, if either, model is correct in the specific case of reaction (3). Reactant Dol is not in oxygen isotope exchange equilibrium with either Fo or Cal in any of the four samples (Fig. 7), inconsistent with the conventional model but consistent with the model of Müller *et al.* (2004). Product Fo and Cal are in oxygen isotope equilibrium in sample KPlL (Fig. 7a), providing further confirmation of the model of Müller *et al.* (2004) in this one sample. In the other three samples, however, Fo and Cal are not in equilibrium (Fig. 7b–d), indicating that the expectations of neither model are generally met.

The problem of missing oxygen isotope alteration

Simple flow models (Fig. 8, Table 4) predict a large region of low-δ^{18}O Dol downstream from the site of reaction (3). No analyzed Dol marble from the Beinn an Dubhaich aureole, however, exhibits the expected depletion (all δ^{18}O = 19·6–22·7‰; Ferry & Rumble, 1997). All but one of 19 analyzed marbles from the Twin Lakes pendant have similar δ^{18}O = 19·4–24·0‰. The single exception is Dol marble sample KPlK, collected within 1 m of sample KPlL, which does have an expected low δ^{18}O = 7·3‰. The models also predict that δ^{18}O(Fo) and δ^{18}O(Cal) should be low, consistent with equilibration with a pluton-derived fluid. The prediction is confirmed in the case of samples KPlL and B43A away from the vein–marble contact (Figs 6 and 7a) and of some Fo grains in sample BlW (Fig. 7d). The prediction is not confirmed, however, in the case of Cal and Fo in sample B4L, of Cal and Fo near the vein–marble contact in sample B43A, and of Cal and some Fo grains in sample BlW (Figs 6b and 7b–d).

The likely explanation for these discrepancies is that the flow models assume *Pe* large enough that oxygen isotope diffusion between sites of Fo growth and reactant Dol can be ignored. At the center of wide flow channels, like the macroscopic veins in samples KPlL and B43A, *h* was large, and mass transport probably was dominated by advection. The assumptions of the flow models are valid, and the predicted low δ^{18}O of Fo and Cal is observed (Figs 6 and 7a). In the matrix of sample B4L, near the vein–marble contact in sample B43A, and in some Fo–Cal segregations in sample BlW, however, *h* was small, and isotope transport between Fo and Dol was probably dominated by diffusion, resulting in δ^{18}O of Cal and Fo controlled by isotope exchange with Dol. Similarly, the absence or small degree of oxygen isotope alteration of most dolomite marbles in the Twin Lakes pendant and Beinn an Dubhaich aureole can be explained if fluids involved in silicification infiltrated rock along thin micrometer-scale cracks or other permeability networks rather than along centimeter-scale veins like those that occur in samples KPlL and B43A.

The problem of missing diopside

Forsterite does not form by direct reaction between Dol and Qtz-saturated fluid (Fig. 8). If fluids that infiltrate Dol are Qtz-saturated, Fo forms by reaction (3) only at points in the model flow systems where most of the silica initially in the fluid has been removed after formation of Di by reaction (4) upstream. For example, along paths la and lb in Fig. 8, 95–96% of SiO_2 initially dissolved in fluid is precipitated by reaction (4) before Fo + Cal forms by reaction (3). For this reason ~10 times as much Di rock as Fo + Cal rock is expected in contact aureoles. Rocks that are pure Di or nearly so, however, are not observed in the Beinn an Dubhaich aureole. Diopside-rich rocks in the Twin Lakes pendant are present but rare. Sample KPlB (Tables 1 and 2) is an example. The sample, however, fails to conform in more detail to the pure Di rocks predicted from the flow models in Fig. 8. First, in addition to Di, the sample contains ~40% Fo + Cal and minor Dol. Second, whereas Di grains contain Fo inclusions (Fig. 11a) consistent with formation of Di by reaction (4), Fo contains Di inclusions (Fig. 11b), indicating that Fo formed to some extent from Di rather than vice versa. Third, the δ^{18}O = 21·5‰ of bulk carbonate in sample KPlB is much greater than the expected low values (Table 4) observed in samples KPlK and KPlL (7–11‰). Some other process evidently occurred during contact metamorphism that played the same role as the formation of Di by reaction (4) in the simple flow models in Fig. 8. The Twin Lakes pendant contains garnet–pyroxene skarns (Chesterman, 1942), and the Beinn an Dubhaich aureole is a classic locality for B–F-rich skarns (Tilley, 1948, 1951). Skarn-forming reactions probably occurred during metamorphism instead of reaction (4). Formation of skarns rather than pure Di would be an inevitable consequence of infiltration of Dol by magmatic fluids that contain many other dissolved metals besides Si.
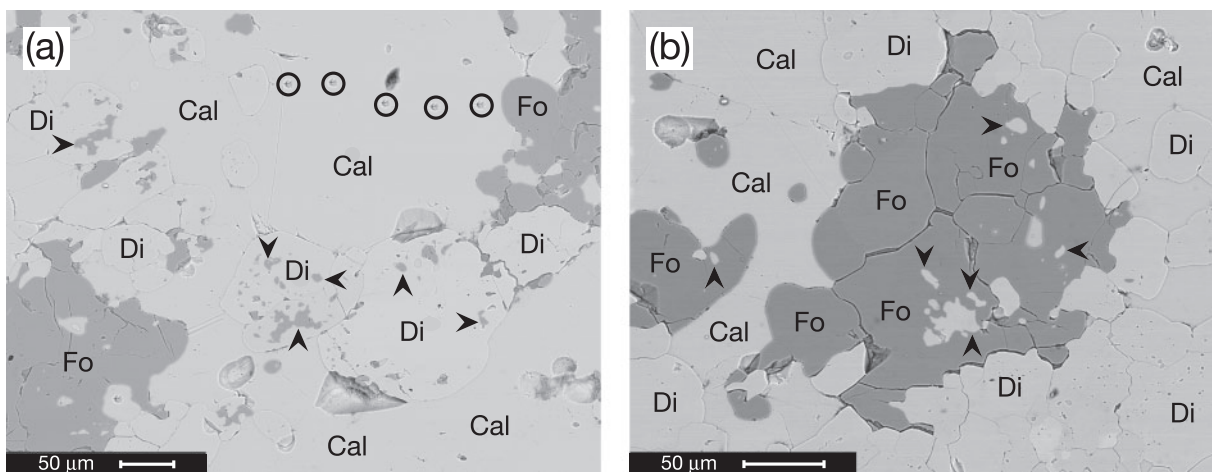
Fig. 11. Backscattered electron micrographs illustrating mineral inclusions in matrix Di and Fo in sample KP1B. (a) Di crystals can contain rounded or amoeboid Fo inclusions (several indicated by black arrowheads) indicating formation of Di from Fo. Spots within black circles are $\sim$5–10 μm diameter pits left from *in situ* measurements of δ^{13}C of Cal by ion microprobe (Ferry *et al.*, 2010). (b) Fo crystals can contain rounded or amoeboid Di inclusions (several indicated by black arrowheads) indicating formation of Fo from Di.

Role of silicification in the formation of periclase

Periclase is an important index mineral in the contact metamorphism of dolomites and defines the Per isograd in numerous aureoles such as Adamello (Müller *et al.*, 2009), Alta (Moore & Kerrick, 1976; Cook & Bowman, 2000), Beinn an Dubhaich (Holness, 1992; Ferry & Rumble, 1997), Monzoni (Masch & Huckenholz, 1993; Ferry *et al.*, 2002), and Predazzo (Ferry *et al.*, 2002). At all these locations Per + Cal formed from Dol by reaction (6), driven by infiltration of Dol marble by chemically reactive, CO_2-poor fluids, derived from or equilibrated with the associated granitic pluton. The fluids, therefore, were probably originally Qtz-saturated. Periclase, however, does not form directly by reaction between Dol and Qtz-saturated fluid (Fig. 8). Periclase forms by reaction (6) only at points in the model flow systems where almost all silica initially in the fluid has been removed by formation of Di by reaction (4) and Fo by the reverse of reaction (5). The fraction of initial dissolved silica that is removed is extreme. Taking flow paths 2a and 2b in Fig. 8 as examples, if the input fluid at the inlet to the flow system is Qtz-saturated, Per develops by reaction (6) only after 99·97–99·99% of the initial dissolved SiO_2 is removed. In contact aureoles, reactions involving formation of skarns or silicification of pure calcite marble to wollastonite are probably involved instead of formation of Di by reaction (4). Silicification of dolomite and limestone during contact metamorphism therefore is an important process not only in the formation of silicate minerals such as Fo, Di, Wo, and other skarn minerals, but also indirectly in the formation of minerals such as Per by reactions that involve no silicate minerals at all.

The broader significance of infiltration-driven mineral reactions during metamorphism

Infiltration-driven decarbonation reactions are common during both contact and regional metamorphism (Ferry & Gerdes, 1998; Baumgartner & Valley, 2001; Ferry *et al.*, 2002; Ague, 2003). As demonstrated in the discussion of Fig. 8, infiltration-driven reactions inevitably proceed at a significant value of reaction affinity. As recognized by Müller *et al.* (2009) and elaborated in this study, the magnitude of reaction affinity depends on X_{CO_2} of the input fluid and thus can vary in both space and time. Because the magnitude of variations in A can be constrained in the case of infiltration-driven decarbonation reactions, these reactions have unexploited potential for developing a quantitatively integrated understanding of mineral reaction, phase equilibria, fluid flow, textures and microstructures, and the redistribution of stable isotopes during metamorphism.

for the bead-like forsterite morphology in samples B43A and B1W.

REFERENCES

Ague, J. J. (2003). Fluid flow in the deep crust. In: Rudnick, R. L. (ed.) *The Crust. Treatise on Geochemistry.* Amsterdam: Elsevier, pp. 195–228.

Anovitz, L. M. & Essene, E. J. (1987). Phase equilibria in the system $CaCO_3–MgCO_3–FeCO_3$. *Journal of Petrology* **28**, 389–414.

Armstrong, J. T. (1988). Quantitative analysis of silicate and oxide minerals: comparison of Monte Carlo, ZAF and phi–rho–z procedures. In: Newbury, D. E. (ed.) *Microbeam Analysis—1988.* San Francisco, CA: San Francisco Press, pp. 239–246.

Baumgartner, L. P. & Valley, J. W. (2001). Stable isotope transport and contact metamorphic fluid flow. In: Valley, J. W. & Cole, D. R. (eds) *Stable Isotope Geochemistry. Mineralogical Society of America and Geochemical Society, Reviews in Mineralogy and Geochemistry* **43**, 415–468.

Begue, F. (2008). Étude des veines métasomatique dans les xénolites carbonates de la bordure de l'intrusion du Bergell, Val Sissone (Italie), M.S. thesis, University of Lausanne.

Berman, R. G. (1988). Internally-consistent thermodynamic data for minerals in the system $Na_2O–K_2O–CaO–MgO–FeO–Fe_2O_3–Al_2O_3–SiO_2–TiO_2–H_2O–CO_2$. *Journal of Petrology* **29**, 445–522.

Bickle, M. J. & McKenzie, D. (1987). The transport of heat and matter by fluids during metamorphism. *Contributions to Mineralogy and Petrology* **95**, 384–392.

Bickle, M. J., Chapman, H. J., Ferry, J. M., Rumble, D. & Fallick, A. E. (1997). Fluid flow and diffusion in the Waterville limestone, south–central Maine: constraints from strontium, oxygen and carbon isotope profiles. *Journal of Petrology* **38**, 1489–1512.

Bowen, N. L. (1940). Progressive metamorphism of siliceous limestone and dolomite. *Journal of Geology* **48**, 225–274.

Bowman, J. R., Valley, J. W. & Kita, N. T. (2009). Mechanisms of oxygen isotope exchange and evolution of $^{18}O/^{16}O$-depleted periclase zone marbles in the Alta aureole, Utah: insights from ion microprobe analysis of calcite. *Contributions to Mineralogy and Petrology* **157**, 77–93.

Bucher, K. (1998). Growth mechanisms of metasomatic reaction veins in dolomite marbles from the Bergell Alps. *Mineralogy and Petrology* **63**, 151–171.

Bucher-Nurminen, K. (1981). The formation of the metasomatic reaction veins in dolomitic marble roof pendants in the Bergell intrusion (Province Sondrio, northern Italy). *American Journal of Science* **281**, 1197–1222.

Bucher-Nurminen, K. (1982). On the mechanism of contact metamorphic aureole formation in dolomitic country rock by the Adamello intrusion (northern Italy). *American Mineralogist* **67**, 1101–1117.

Carmichael, S. K., Ferry, J. M. & McDonough, W. F. (2008). Formation of replacement dolomite in the Latemar carbonate buildup, northern Italy: part 1. Field relations, mineralogy, and geochemistry. *American Journal of Science* **308**, 851–884.

Chacko, T., Cole, D. R. & Horita, J. (2001). Equilibrium oxygen, hydrogen, and carbon isotope fractionation factors applicable to geologic systems. In: Valley, J. W. & Cole, D. R. (eds) *Stable Isotope Geochemistry. Mineralogical Society of America and Geochemical Society, Reviews in Mineralogy and Geochemistry* **43**, 1–81.

Chamberlain, C. P., Ferry, J. M. & Rumble, D. (1990). The effect of net-transfer reactions on the isotopic compositions of minerals. *Contributions to Mineralogy and Petrology* **105**, 322–336.

Chesterman, C. W. (1942). Contact metamorphism in the Twin Lakes region, Fresno County, California. *California Journal of Mines and Geology* **38**, 243–281.

Cook, S. J. & Bowman, J. R. (2000). Mineralogical evidence for fluid–rock interaction accompanying prograde contact metamorphism of siliceous dolomites: Alta aureole, Utah, USA. *Journal of Petrology* **41**, 739–757.

Davis, S. R. & Ferry, J. M. (1993). Fluid infiltration during contact metamorphism of interbedded marble and calc-silicate hornfels, Twin Lakes area, central Sierra Nevada, California. *Journal of Metamorphic Geology* **11**, 71–88.

Dipple, G. M. & Ferry, J. M. (1992). Fluid flow and stable isotopic alteration of rocks at elevated temperatures with applications to metamorphism. *Geochimica et Cosmochimica Acta* **56**, 3539–3550.

Ferry, J. M. (1994). Role of fluid flow in the contact metamorphism of siliceous dolomitic limestones. *American Mineralogist* **79**, 719–736.

Ferry, J. M. (1996a). Prograde and retrograde fluid flow during contact metamorphism of siliceous carbonate rocks from the Ballachulish aureole, Scotland. *Contributions to Mineralogy and Petrology* **124**, 235–254.

Ferry, J. M. (1996b). Three novel isograds in metamorphosed siliceous dolomites from the Ballachulish aureole, Scotland. *American Mineralogist* **81**, 485–494.

Ferry, J. M. (2001). Calcite inclusions in forsterite. *American Mineralogist* **86**, 773–779.

Ferry, J. M. & Gerdes, M. (1998). Chemically reactive fluid flow during metamorphism. *Annual Review of Earth and Planetary Sciences* **26**, 255–287.

Ferry, J. M. & Rumble, D. (1997). Formation and destruction of periclase by fluid flow in two contact aureoles. *Contributions to Mineralogy and Petrology* **128**, 313–334.

Ferry, J. M., Sorensen, S. S. & Rumble, D. (1998). Structurally controlled fluid flow during contact metamorphism in the Ritter Range pendant, California, USA. *Contributions to Mineralogy and Petrology* **130**, 358–378.

Ferry, J. M., Wing, B. A., Penniston-Dorland, S. C. & Rumble, D. (2002). The direction of fluid flow during contact metamorphism of siliceous carbonate rocks: new data for the Monzoni and Predazzo aureoles, northern Italy, and a global review. *Contributions to Mineralogy and Petrology* **142**, 679–699.

Ferry, J. M., Ushikubo, T., Kita, N. T. & Valley, J. W. (2010). Assessment of grain-scale homogeneity of carbon and oxygen isotope compositions of minerals in carbonate-bearing metamorphic rocks by ion microprobe. *Geochimica et Cosmochimica Acta* **74**, 6517–6540.

Fournier, R. O. & Potter, R. W., II (1982). An equation correlating the solubility of quartz in water from 25°C to 900°C at pressures up to 10,000 bars. *Geochimica et Cosmochimica Acta* **46**, 1969–1973.

Holland, T. J. B. & Powell, R. (1998). An internally consistent thermodynamic data set for phases of petrological interest. *Journal of Metamorphic Geology* **16**, 309–343.

Holness, M. B. (1990). Experimental and petrological studies of textural equilibration and fluid flow in metacarbonate rocks: the Beinn an Dubhaich aureole, Skye, Ph.D. thesis, University of Cambridge.

Holness, M. B. (1992). Metamorphism and fluid infiltration of the calc-silicate aureole of the Beinn an Dubhaich granite, Skye. *Journal of Petrology* **33**, 1261–1293.

Holness, M. B. (1997). Fluid flow paths and mechanisms of fluid infiltration in carbonates during contact metamorphism: the Beinn an Dubhaich aureole, Skye. *Journal of Metamorphic Geology* **15**, 59–70.

Holness, M. B. & Fallick, A. E. (1997). Palaeohydrology of the calcsilicate aureole of the Beinn an Dubhaich granite, Skye, Scotland: a stable isotopic study. *Journal of Metamorphic Geology* **15**, 71–83.

Holness, M. B. & Siklos, S. T. C. (2000). The rates and extent of textural equilibration in high-temperature fluid-bearing systems. *Chemical Geology* **162**, 137–153.

Holness, M. B., Bickle, M. J. & Graham, C. M. (1991). On the kinetics of textural equilibration in forsterite marbles. *Contributions to Mineralogy and Petrology* **108**, 356–367.

Kerrick, D. M. & Jacobs, G. K. (1981). A modified Redlich–Kwong equation for H_2O, CO_2, and $H_2O–CO_2$ mixtures at elevated pressures and temperatures. *American Journal of Science* **281**, 735–767.

Kerrick, D. M., Crawford, K. W. & Randazzo, A. F. (1973). Metamorphism of calcareous rocks in three roof pendants in the Sierra Nevada, California. *Journal of Petrology* **14**, 303–325.

Kita, N. T., Ushikubo, T., Fu, B. & Valley, J. W. (2009). High precision SIMS oxygen isotope analyses and the effect of topography. *Chemical Geology* **264**, 43–57.

Kita, N. T., Nagahara, H., Tachibana, S., Tomomura, S., Spicuzza, M. J., Fournelle, J. H. & Valley, J. W. (2010). High precision SIMS oxygen three isotope study of chondrules in LL3 chondrites: role of ambient gas during chondrule formation. *Geochimica et Cosmochimica Acta* **74**, 6610–6635.

Kozdon, R., Ushikubo, T., Kita, N. T. & Valley, J. W. (2009). Intratest oxygen isotope variability in planktonic foraminifera: new insights from *in situ* measurement by ion microprobe. *Chemical Geology* **258**, 327–337.

Mahon, K. I. (1996). The new 'York' regression: application of an improved statistical method to geochemistry. *International Geology Review* **38**, 293–303.

Masch, L. & Huckenholz, H. G. (1993). Der Intrusivkomplex von Monzoni und seine thermometamorphe Aureole. *Beihilfe European Journal of Mineralogy* **5**, 81–135.

Moorbath, S. & Bell, J. D. (1965). Strontium isotope abundance studies and rubidium–strontium age determinations on Tertiary rocks from the Isle of Skye, north-west Scotland. *Journal of Petrology* **6**, 37–66.

Moore, J. N. & Kerrick, D. M. (1976). Equilibria in siliceous dolomites of the Alta aureole, Utah. *American Journal of Science* **276**, 502–524.

Müller, T., Baumgartner, L. P., Foster, C. T., Jr & Vennemann, T. W. (2004). Metastable prograde mineral reactions in contact aureoles. *Geology* **32**, 821–824.

Müller, T., Baumgartner, L. P., Foster, C. T., Jr & Bowman, J. R. (2009). Crystal size distribution of periclase in contact metamorphic dolomite marbles from the southern Adamello Massif, Italy. *Journal of Petrology* **50**, 451–465.

Newton, R. C. & Manning, C. E. (2009). Hydration state and activity of aqueous silica in $H_2O–CO_2$ fluids at high pressure and temperature. *American Mineralogist* **94**, 1287–1290.

Penniston-Dorland, S. C. & Ferry, J. M. (2006). Development of spatial variations in reaction progress during regional metamorphism of micaceous carbonate rocks, northern New England. *American Journal of Science* **306**, 475–524.

Roselle, G. T. (1997). Integrated petrologic, stable isotopic, and statistical study of fluid-flow in carbonates of the Ubehebe Peak contact aureole, Death Valley National Park, California, Ph.D. thesis, University of Wisconsin, Madison.

Roselle, G. T., Baumgartner, L. P. & Chapman, J. A. (1997). Nucleation-dominated crystallization of forsterite in the Ubehebe Peak contact aureole, California. *Geology* **25**, 823–826.

Rumble, D. (1982). Stable isotope fractionation during metamorphic devolatilization reactions. In: Ferry, J. M. (ed.) *Characterization of Metamorphism through Mineral Equilibria. Mineralogical Society of America, Reviews in Mineralogy* **10**, 327–353.

Skippen, G. B. (1974). An experimental model for low pressure metamorphism of siliceous dolomite marble. *American Journal of Science* **274**, 487–509.

Stern, J. W., Bateman, P. C., Morgan, B. A., Newell, M. F. & Peck, D. L. (1981). *Isotopic U–Pb ages of zircon from the granitoids of the central Sierra Nevada, California. US Geological Survey, Professional Papers* **1185**.

Tilley, C. E. (1948). Dolomite contact skarns of the Broadford area, Skye: a preliminary note. *Geological Magazine* **85**, 213–216.

Tilley, C. E. (1951). The zoned contact skarns of the Broadford area, Skye: a study of boron–fluorine metasomatism in dolomites. *Mineralogical Magazine* **29**, 621–665.

Valley, J. W. (1986). Stable isotope geochemistry of metamorphic rocks. In: Valley, J. W., Taylor, H. P., Jr & O'Neil, J. R. (eds) *Stable Isotopes in High Temperature Geological Processes. Mineralogical Society of America, Reviews in Mineralogy* **16**, 445–490.

Valley, J. W. & Kita, N. T. (2009). *In situ* oxygen isotope geochemistry by ion microprobe. In: Fayek, M. (ed.) *Secondary Ion Mass Spectrometry in the Earth Sciences. Mineralogical Association of Canada Short Course* **41**, 19–63.

Walther, J. V. & Wood, B. J. (1986). Mineral–fluid reaction rates. In: Walther, J. V. & Wood, B. J. (eds) *Fluid–Rock Interactions during Metamorphism*. Berlin: Springer, pp. 194–211.

Watson, E. B. & Müller, T. (2009). Non-equilibrium isotopic and elemental fractionation during diffusion-controlled crystal growth under static and dynamic conditions. *Chemical Geology* **267**, 111–124.

Wing, B. A., Ferry, J. M. & Rumble, D. (2000). Controls on porosity development during contact metamorphism. *Geological Society of America, Programs with Abstracts* **32**, A295.